Study of *CP* violation in Dalitz-plot analyses of $B^0 \to K^+K^-K^0_S$, $B^+ \to K^+K^-K^+$, and $B^+ \to K^0_S K^0_S K^+$

J. P. Lees,[1] V. Poireau,[1] V. Tisserand,[1] J. Garra Tico,[2] E. Grauges,[2] D. A. Milanes,[3] A. Palano,[3,4] M. Pappagallo,[3,4] G. Eigen,[5] B. Stugu,[5] D. N. Brown,[6] L. T. Kerth,[6] Yu. G. Kolomensky,[6] G. Lynch,[6] H. Koch,[7] T. Schroeder,[7] D. J. Asgeirsson,[8] C. Hearty,[8] T. S. Mattison,[8] J. A. McKenna,[8] A. Khan,[9] V. E. Blinov,[10] A. R. Buzykaev,[10] V. P. Druzhinin,[10] V. B. Golubev,[10] E. A. Kravchenko,[10] A. P. Onuchin,[10] S. I. Serednyakov,[10] Yu. I. Skovpen,[10] E. P. Solodov,[10] K. Yu. Todyshev,[10] A. N. Yushkov,[10] M. Bondioli,[11] D. Kirkby,[11] A. J. Lankford,[11] M. Mandelkern,[11] H. Atmacan,[12] J. W. Gary,[12] F. Liu,[12] O. Long,[12] G. M. Vitug,[12] C. Campagnari,[13] T. M. Hong,[13] D. Kovalskyi,[13] J. D. Richman,[13] C. A. West,[13] A. M. Eisner,[14] J. Kroseberg,[14] W. S. Lockman,[14] A. J. Martinez,[14] T. Schalk,[14] B. A. Schumm,[14] A. Seiden,[14] D. S. Chao,[15] C. H. Cheng,[15] D. A. Doll,[15] B. Echenard,[15] K. T. Flood,[15] D. G. Hitlin,[15] P. Ongmongkolkul,[15] F. C. Porter,[15] A. Y. Rakitin,[15] R. Andreassen,[16] Z. Huard,[16] B. T. Meadows,[16] M. D. Sokoloff,[16] L. Sun,[16] P. C. Bloom,[17] W. T. Ford,[17] A. Gaz,[17] M. Nagel,[17] U. Nauenberg,[17] J. G. Smith,[17] S. R. Wagner,[17] R. Ayad,[18,*] W. H. Toki,[18] B. Spaan,[19] M. J. Kobel,[20] K. R. Schubert,[20] R. Schwierz,[20] D. Bernard,[21] M. Verderi,[21] P. J. Clark,[22] S. Playfer,[22] D. Bettoni,[23] C. Bozzi,[23] R. Calabrese,[23,24] G. Cibinetto,[23,24] E. Fioravanti,[23,24] I. Garzia,[23,24] E. Luppi,[23,24] M. Munerato,[23,24] M. Negrini,[23,24] L. Piemontese,[23] V. Santoro,[23] R. Baldini-Ferroli,[25] A. Calcaterra,[25] R. de Sangro,[25] G. Finocchiaro,[25] P. Patteri,[25] I. M. Peruzzi,[25,†] M. Piccolo,[25] M. Rama,[25] A. Zallo,[25] R. Contri,[26,27] E. Guido,[26,27] M. Lo Vetere,[26,27] M. R. Monge,[26,27] S. Passaggio,[26] C. Patrignani,[26,27] E. Robutti,[26] B. Bhuyan,[28] V. Prasad,[28] C. L. Lee,[29] M. Morii,[29] A. J. Edwards,[30] A. Adametz,[31] J. Marks,[31] U. Uwer,[31] H. M. Lacker,[32] T. Lueck,[32] P. D. Dauncey,[33] P. K. Behera,[34] U. Mallik,[34] C. Chen,[35] J. Cochran,[35] W. T. Meyer,[35] S. Prell,[35] A. E. Rubin,[35] A. V. Gritsan,[36] Z. J. Guo,[36] N. Arnaud,[37] M. Davier,[37] D. Derkach,[37] G. Grosdidier,[37] F. Le Diberder,[37] A. M. Lutz,[37] B. Malaescu,[37] P. Roudeau,[37] M. H. Schune,[37] A. Stocchi,[37] G. Wormser,[37] D. J. Lange,[38] D. M. Wright,[38] I. Bingham,[39] C. A. Chavez,[39] J. P. Coleman,[39] J. R. Fry,[39] E. Gabathuler,[39] D. E. Hutchcroft,[39] D. J. Payne,[39] C. Touramanis,[39] A. J. Bevan,[40] F. Di Lodovico,[40] R. Sacco,[40] M. Sigamani,[40] G. Cowan,[41] D. N. Brown,[42] C. L. Davis,[42] A. G. Denig,[43] M. Fritsch,[43] W. Gradl,[43] A. Hafner,[43] E. Prencipe,[43] D. Bailey,[44] R. J. Barlow,[44,‡] G. Jackson,[44] G. D. Lafferty,[44] E. Behn,[45] R. Cenci,[45] B. Hamilton,[45] A. Jawahery,[45] D. A. Roberts,[45] G. Simi,[45] C. Dallapiccola,[46] R. Cowan,[47] D. Dujmic,[47] G. Sciolla,[47] R. Cheaib,[48] D. Lindemann,[48] P. M. Patel,[48] S. H. Robertson,[48] M. Schram,[48] P. Biassoni,[49,50] N. Neri,[49] F. Palombo,[49,50] S. Stracka,[49,50] L. Cremaldi,[51] R. Godang,[51,§] R. Kroeger,[51] P. Sonnek,[51] D. J. Summers,[51] X. Nguyen,[52] M. Simard,[52] P. Taras,[52] G. De Nardo,[53,54] D. Monorchio,[53,54] G. Onorato,[53,54] C. Sciacca,[53,54] M. Martinelli,[55] G. Raven,[55] C. P. Jessop,[56] K. J. Knoepfel,[56] J. M. LoSecco,[56] W. F. Wang,[56] K. Honscheid,[57] R. Kass,[57] J. Brau,[58] R. Frey,[58] N. B. Sinev,[58] D. Strom,[58] E. Torrence,[58] E. Feltresi,[59,60] N. Gagliardi,[59,60] M. Margoni,[59,60] M. Morandin,[59] M. Posocco,[59] M. Rotondo,[59] F. Simonetto,[59,60] R. Stroili,[59,60] S. Akar,[61] E. Ben-Haim,[61] M. Bomben,[61] G. R. Bonneaud,[61] H. Briand,[61] G. Calderini,[61] J. Chauveau,[61] O. Hamon,[61] Ph. Leruste,[61] G. Marchiori,[61] J. Ocariz,[61] S. Sitt,[61] M. Biasini,[62,63] E. Manoni,[62,63] S. Pacetti,[62,63] A. Rossi,[62,63] C. Angelini,[64,65] G. Batignani,[64,65] S. Bettarini,[64,65] M. Carpinelli,[64,65,‖] G. Casarosa,[64,65] A. Cervelli,[64,65] F. Forti,[64,65] M. A. Giorgi,[64,65] A. Lusiani,[64,65] B. Oberhof,[64,65] E. Paoloni,[64,65] A. Perez,[64] G. Rizzo,[64,65] J. J. Walsh,[64] D. Lopes Pegna,[67] J. Olsen,[67] A. J. S. Smith,[67] A. V. Telnov,[67] F. Anulli,[68] G. Cavoto,[68] R. Faccini,[68,69] F. Ferrarotto,[68] F. Ferroni,[68] L. Li Gioi,[68] M. A. Mazzoni,[68] G. Piredda,[68] C. Bünger,[70] O. Grünberg,[70] T. Hartmann,[70] T. Leddig,[70] H. Schröder,[70] C. Voss,[70] R. Waldi,[70] T. Adye,[71] E. O. Olaiya,[71] F. F. Wilson,[71] S. Emery,[72] G. Hamel de Monchenault,[72] G. Vasseur,[72] Ch. Yèche,[72] D. Aston,[73] D. J. Bard,[73] R. Bartoldus,[73] C. Cartaro,[73] M. R. Convery,[73] J. Dorfan,[73] G. P. Dubois-Felsmann,[73] W. Dunwoodie,[73] M. Ebert,[73] R. C. Field,[73] M. Franco Sevilla,[73] B. G. Fulsom,[73] A. M. Gabareen,[73] M. T. Graham,[73] P. Grenier,[73] C. Hast,[73] W. R. Innes,[73] M. H. Kelsey,[73] P. Kim,[73] M. L. Kocian,[73] D. W. G. S. Leith,[73] P. Lewis,[73] B. Lindquist,[73] S. Luitz,[73] V. Luth,[73] H. L. Lynch,[73] D. B. MacFarlane,[73] D. R. Muller,[73] H. Neal,[73] S. Nelson,[73] M. Perl,[73] T. Pulliam,[73] B. N. Ratcliff,[73] A. Roodman,[73] A. A. Salnikov,[73] R. H. Schindler,[73] A. Snyder,[73] D. Su,[73] M. K. Sullivan,[73] J. Va'vra,[73] A. P. Wagner,[73] M. Weaver,[73] W. J. Wisniewski,[73] M. Wittgen,[73] D. H. Wright,[73] H. W. Wulsin,[73] C. C. Young,[73] V. Ziegler,[73] W. Park,[74] M. V. Purohit,[74] R. M. White,[74] J. R. Wilson,[74] A. Randle-Conde,[74] S. J. Sekula,[75] M. Bellis,[76] J. F. Benitez,[76] P. R. Burchat,[76] T. S. Miyashita,[76] M. S. Alam,[77] J. A. Ernst,[77] R. Gorodeisky,[78] N. Guttman,[78] D. R. Peimer,[78] A. Soffer,[78] P. Lund,[79] S. M. Spanier,[79] R. Eckmann,[80] J. L. Ritchie,[80] A. M. Ruland,[80] C. J. Schilling,[80] R. F. Schwitters,[80] B. C. Wray,[80] J. M. Izen,[81] X. C. Lou,[81] F. Bianchi,[82,83] D. Gamba,[82,83] L. Lanceri,[84,85] L. Vitale,[84,85] F. Martinez-Vidal,[86] A. Oyanguren,[86] H. Ahmed,[87] J. Albert,[87] Sw. Banerjee,[87] F. U. Bernlochner,[87] H. H. F. Choi,[87]

G. J. King,[87] R. Kowalewski,[87] M. J. Lewczuk,[87] I. M. Nugent,[87] J. M. Roney,[87] R. J. Sobie,[87] N. Tasneem,[87] T. J. Gershon,[88] P. F. Harrison,[88] T. E. Latham,[88] E. M. T. Puccio,[88] H. R. Band,[89] S. Dasu,[89] Y. Pan,[89] R. Prepost,[89] and S. L. Wu[89]

(*BABAR* Collaboration)

[1]*Laboratoire d'Annecy-le-Vieux de Physique des Particules (LAPP), Université de Savoie, CNRS/IN2P3, F-74941 Annecy-Le-Vieux, France*
[2]*Universitat de Barcelona, Facultat de Fisica, Departament ECM, E-08028 Barcelona, Spain*
[3]*INFN Sezione di Bari, I-70126 Bari, Italy*
[4]*Dipartimento di Fisica, Università di Bari, I-70126 Bari, Italy*
[5]*University of Bergen, Institute of Physics, N-5007 Bergen, Norway*
[6]*Lawrence Berkeley National Laboratory and University of California, Berkeley, California 94720, USA*
[7]*Ruhr Universität Bochum, Institut für Experimentalphysik 1, D-44780 Bochum, Germany*
[8]*University of British Columbia, Vancouver, British Columbia, Canada V6T 1Z1*
[9]*Brunel University, Uxbridge, Middlesex UB8 3PH, United Kingdom*
[10]*Budker Institute of Nuclear Physics, Novosibirsk 630090, Russia*
[11]*University of California at Irvine, Irvine, California 92697, USA*
[12]*University of California at Riverside, Riverside, California 92521, USA*
[13]*University of California at Santa Barbara, Santa Barbara, California 93106, USA*
[14]*University of California at Santa Cruz, Institute for Particle Physics, Santa Cruz, California 95064, USA*
[15]*California Institute of Technology, Pasadena, California 91125, USA*
[16]*University of Cincinnati, Cincinnati, Ohio 45221, USA*
[17]*University of Colorado, Boulder, Colorado 80309, USA*
[18]*Colorado State University, Fort Collins, Colorado 80523, USA*
[19]*Technische Universität Dortmund, Fakultät Physik, D-44221 Dortmund, Germany*
[20]*Technische Universität Dresden, Institut für Kern- und Teilchenphysik, D-01062 Dresden, Germany*
[21]*Laboratoire Leprince-Ringuet, Ecole Polytechnique, CNRS/IN2P3, F-91128 Palaiseau, France*
[22]*University of Edinburgh, Edinburgh EH9 3JZ, United Kingdom*
[23]*INFN Sezione di Ferrara, I-44100 Ferrara, Italy*
[24]*Dipartimento di Fisica, Università di Ferrara, I-44100 Ferrara, Italy*
[25]*INFN Laboratori Nazionali di Frascati, I-00044 Frascati, Italy*
[26]*INFN Sezione di Genova, I-16146 Genova, Italy*
[27]*Dipartimento di Fisica, Università di Genova, I-16146 Genova, Italy*
[28]*Indian Institute of Technology Guwahati, Guwahati, Assam, 781 039, India*
[29]*Harvard University, Cambridge, Massachusetts 02138, USA*
[30]*Harvey Mudd College, Claremont, California 91711*
[31]*Universität Heidelberg, Physikalisches Institut, Philosophenweg 12, D-69120 Heidelberg, Germany*
[32]*Humboldt-Universität zu Berlin, Institut für Physik, Newtonstrasse 15, D-12489 Berlin, Germany*
[33]*Imperial College London, London, SW7 2AZ, United Kingdom*
[34]*University of Iowa, Iowa City, Iowa 52242, USA*
[35]*Iowa State University, Ames, Iowa 50011-3160, USA*
[36]*Johns Hopkins University, Baltimore, Maryland 21218, USA*
[37]*Laboratoire de l'Accélérateur Linéaire, IN2P3/CNRS et Université Paris-Sud 11, Centre Scientifique d'Orsay, B. P. 34, F-91898 Orsay Cedex, France*
[38]*Lawrence Livermore National Laboratory, Livermore, California 94550, USA*
[39]*University of Liverpool, Liverpool L69 7ZE, United Kingdom*
[40]*Queen Mary, University of London, London, E1 4NS, United Kingdom*
[41]*University of London, Royal Holloway and Bedford New College, Egham, Surrey TW20 0EX, United Kingdom*
[42]*University of Louisville, Louisville, Kentucky 40292, USA*
[43]*Johannes Gutenberg-Universität Mainz, Institut für Kernphysik, D-55099 Mainz, Germany*
[44]*University of Manchester, Manchester M13 9PL, United Kingdom*
[45]*University of Maryland, College Park, Maryland 20742, USA*
[46]*University of Massachusetts, Amherst, Massachusetts 01003, USA*
[47]*Massachusetts Institute of Technology, Laboratory for Nuclear Science, Cambridge, Massachusetts 02139, USA*
[48]*McGill University, Montréal, Québec, Canada H3A 2T8*
[49]*INFN Sezione di Milano, I-20133 Milano, Italy*
[50]*Dipartimento di Fisica, Università di Milano, I-20133 Milano, Italy*
[51]*University of Mississippi, University, Mississippi 38677, USA*

[52]*Université de Montréal, Physique des Particules, Montréal, Québec, Canada H3C 3J7*
[53]*INFN Sezione di Napoli, I-80126 Napoli, Italy*
[54]*Dipartimento di Scienze Fisiche, Università di Napoli Federico II, I-80126 Napoli, Italy*
[55]*NIKHEF, National Institute for Nuclear Physics and High Energy Physics, NL-1009 DB Amsterdam, The Netherlands*
[56]*University of Notre Dame, Notre Dame, Indiana 46556, USA*
[57]*The Ohio State University, Columbus, Ohio 43210, USA*
[58]*University of Oregon, Eugene, Oregon 97403, USA*
[59]*INFN Sezione di Padova, I-35131 Padova, Italy*
[60]*Dipartimento di Fisica, Università di Padova, I-35131 Padova, Italy*
[61]*Laboratoire de Physique Nucléaire et de Hautes Energies, IN2P3/CNRS, Université Pierre et Marie Curie-Paris6, Université Denis Diderot-Paris7, F-75252 Paris, France*
[62]*INFN Sezione di Perugia, I-06100 Perugia, Italy*
[63]*Dipartimento di Fisica, Università di Perugia, I-06100 Perugia, Italy*
[64]*INFN Sezione di Pisa, I-56127 Pisa, Italy*
[65]*Dipartimento di Fisica, Università di Pisa, I-56127 Pisa, Italy*
[66]*Scuola Normale Superiore di Pisa, I-56127 Pisa, Italy*
[67]*Princeton University, Princeton, New Jersey 08544, USA*
[68]*INFN Sezione di Roma, I-00185 Roma, Italy*
[69]*Dipartimento di Fisica, Università di Roma La Sapienza, I-00185 Roma, Italy*
[70]*Universität Rostock, D-18051 Rostock, Germany*
[71]*Rutherford Appleton Laboratory, Chilton, Didcot, Oxon, OX11 0QX, United Kingdom*
[72]*CEA, Irfu, SPP, Centre de Saclay, F-91191 Gif-sur-Yvette, France*
[73]*SLAC National Accelerator Laboratory, Stanford, California 94309 USA*
[74]*University of South Carolina, Columbia, South Carolina 29208, USA*
[75]*Southern Methodist University, Dallas, Texas 75275, USA*
[76]*Stanford University, Stanford, California 94305-4060, USA*
[77]*State University of New York, Albany, New York 12222, USA*
[78]*Tel Aviv University, School of Physics and Astronomy, Tel Aviv, 69978, Israel*
[79]*University of Tennessee, Knoxville, Tennessee 37996, USA*
[80]*University of Texas at Austin, Austin, Texas 78712, USA*
[81]*University of Texas at Dallas, Richardson, Texas 75083, USA*
[82]*INFN Sezione di Torino, I-10125 Torino, Italy*
[83]*Dipartimento di Fisica Sperimentale, Università di Torino, I-10125 Torino, Italy*
[84]*INFN Sezione di Trieste, I-34127 Trieste, Italy*
[85]*Dipartimento di Fisica, Università di Trieste, I-34127 Trieste, Italy*
[86]*IFIC, Universitat de Valencia-CSIC, E-46071 Valencia, Spain*
[87]*University of Victoria, Victoria, British Columbia, Canada V8W 3P6*
[88]*Department of Physics, University of Warwick, Coventry CV4 7AL, United Kingdom*
[89]*University of Wisconsin, Madison, Wisconsin 53706, USA*
(Received 31 January 2012; published 22 June 2012)

We perform amplitude analyses of the decays $B^0 \to K^+K^-K^0_S$, $B^+ \to K^+K^-K^+$, and $B^+ \to K^0_SK^0_SK^+$, and measure *CP*-violating parameters and partial branching fractions. The results are based on a data sample of approximately 470×10^6 $B\bar{B}$ decays, collected with the *BABAR* detector at the PEP-II asymmetric-energy B factory at the SLAC National Accelerator Laboratory. For $B^+ \to K^+K^-K^+$, we find a direct *CP* asymmetry in $B^+ \to \phi(1020)K^+$ of $A_{CP} = (12.8 \pm 4.4 \pm 1.3)\%$, which differs from zero by 2.8σ. For $B^0 \to K^+K^-K^0_S$, we measure the *CP*-violating phase $\beta_{\rm eff}(\phi(1020)K^0_S) = (21 \pm 6 \pm 2)^\circ$. For $B^+ \to K^0_SK^0_SK^+$, we measure an overall direct *CP* asymmetry of $A_{CP} = (4^{+4}_{-5} \pm 2)\%$. We also perform an angular-moment analysis of the three channels and determine that the $f_X(1500)$ state can be described well by the sum of the resonances $f_0(1500)$, $f'_2(1525)$, and $f_0(1710)$.

DOI: 10.1103/PhysRevD.85.112010 PACS numbers: 13.25.Hw, 13.25.Jx, 13.66.Bc, 14.40.Nd

[*]Now at the University of Tabuk, Tabuk 71491, Saudi Arabia.
[†]Also with Università di Perugia, Dipartimento di Fisica, Perugia, Italy.
[‡]Now at the University of Huddersfield, Huddersfield HD1 3DH, UK.
[§]Now at University of South Alabama, Mobile, AL 36688, USA.
[‖]Also with Università di Sassari, Sassari, Italy.

I. INTRODUCTION

In the standard model (SM), CP violation in the quark sector is entirely described by a single weak phase in the Cabibbo-Kobayashi-Maskawa (CKM) quark-mixing matrix. Studies of time-dependent CP violation in $B^0 \to (c\bar{c})K^0$ decay[1] have yielded precise measurements [1,2] of $\sin 2\beta$, where $\beta \equiv \arg[-(V_{cb}^* V_{cd})/(V_{tb}^* V_{td})]$ and V_{ij} are the elements of the CKM matrix. Measurements of time-dependent CP violation in $b \to q\bar{q}s$ ($q = u, d, s$) decays offer an alternative method for measuring β. Such decays are dominated by $b \to s$ loop diagrams, and therefore are sensitive to possible new physics (NP) contributions appearing in the loops of these diagrams. As a result, the effective β ($\beta_{\rm eff}$) measured in such decays could differ from the β measured in $B^0 \to (c\bar{c})K^0$. Deviations of $\beta_{\rm eff}$ from β are also possible in the SM, due to additional amplitudes from $b \to u$ tree diagrams, loop diagrams containing different CKM factors ("u penguins"), and final-state interactions.

The decay mode $B^0 \to \phi K_S^0$ is particularly suited for a NP search, as $\beta_{\rm eff}$ for this mode is expected to be very near in value to β in the SM, with $\sin 2\beta_{\rm eff} - \sin 2\beta$ in the range $(-0.01, 0.04)$ [3–5]. However, the measurement of $\beta_{\rm eff}$ is complicated due to other $B^0 \to K^+K^-K_S^0$ decays that interfere with $B^0 \to \phi K_S^0$. In general, $K^+K^-K_S^0$ is not a CP eigenstate: the $K^+K^-K_S^0$ system is CP even (odd) if the K^+K^- system has even (odd) angular momentum. Thus, one must account for the (mostly S-wave) $K^+K^-K_S^0$ states that interfere with ϕK_S^0. This can be done by measuring $\beta_{\rm eff}$ using a Dalitz-plot (DP) analysis of $B^0 \to K^+K^-K_S^0$. A further benefit of a DP analysis is that it allows both $\sin 2\beta_{\rm eff}$ and $\cos 2\beta_{\rm eff}$ to be determined, through the interference of odd and even partial waves, which eliminates a trigonometric ambiguity between $\beta_{\rm eff}$ and $90^\circ - \beta_{\rm eff}$.

The related decay mode $B^+ \to \phi K^+$ is another interesting channel in which to search for NP. This decay is also dominated by a $b \to s$ penguin amplitude, and its direct CP asymmetry, A_{CP}, is predicted to be small in the SM, (0.0–4.7)% [5,6], so a significant deviation from zero could be a signal of NP.

In addition to measuring $\beta_{\rm eff}$ in $B^0 \to \phi K_S^0$, it is possible to measure it for the other resonant and nonresonant $B^0 \to K^+K^-K_S^0$ decays. However, these decays may contain a mixture of even and odd partial waves, so the final state is not guaranteed to be a CP eigenstate, thus posing a challenge to a measurement of $\beta_{\rm eff}$. A DP analysis can reveal which partial waves are present, thus eliminating a source of systematic uncertainty affecting the extraction of $\beta_{\rm eff}$, without having to rely on theoretical predictions.

Previous analyses of $B^+ \to K^+K^-K^+$ [7,8] and $B^0 \to K^+K^-K_S^0$ [9,10] have revealed a complex DP structure that is poorly understood. Both modes exhibit a large peak around $m(K^+K^-) \sim 1500\ {\rm MeV}/c^2$, which has been dubbed the $f_X(1500)$. Both *BABAR* and Belle have modeled it as a scalar resonance. The recent DP analysis of $B^0 \to K_S^0K_S^0K_S^0$ by *BABAR* [11] does not yield evidence for this resonance. It is important to clarify the properties of the $f_X(1500)$ with a larger data sample, and, in particular, to determine its spin, as that affects the $\beta_{\rm eff}$ measurement in $B^0 \to K^+K^-K_S^0$.

An additional feature seen in $B^0 \to K^+K^-K_S^0$ and $B^+ \to K^+K^-K^+$ decays is a large broad "nonresonant" (NR) contribution. Previous analyses have found that a uniform-phase-space model is insufficient to describe the NR term, and have instead parametrized it with an empirical model. The NR term has been taken to be purely K^+K^- S wave in $B^+ \to K^+K^-K^+$ [7,8], while smaller $K^+K_S^0$ and $K^-K_S^0$ S-wave terms have been seen in $B^0 \to K^+K^-K_S^0$ [9,10], which correspond effectively to higher-order K^+K^- partial waves. Because the NR contribution dominates much of the available phase space, it is crucial to study its angular distribution if one wishes to accurately measure $\beta_{\rm eff}$ over the entire $B^0 \to K^+K^-K_S^0$ DP.

Because of the importance of understanding the DP structure in $B^0 \to K^+K^-K_S^0$, we study the related modes $B^+ \to K^+K^-K^+$ and $B^+ \to K_S^0K_S^0K^+$ along with $B^0 \to K^+K^-K_S^0$. The mode $B^+ \to K^+K^-K^+$ is valuable because it has the most signal events by far of any $B \to KKK$ mode. Far fewer events are expected in $B^+ \to K_S^0K_S^0K^+$, but its DP has a simplified spin structure due to the fact that the two K_S^0 mesons in the final state are forbidden (by Bose-Einstein statistics) to be in an odd angular momentum configuration. This implies that the $f_X(1500)$ can decay to $K_S^0K_S^0$ only if it has even spin, and it also ensures that the nonresonant component in $B^+ \to K_S^0K_S^0K^+$ does not contain any $K_S^0K_S^0$ P-wave contribution.

In this paper we report the results of DP analyses of $B^+ \to K^+K^-K^+$ and $B^+ \to K_S^0K_S^0K^+$, and a time-dependent DP analysis of $B^0 \to K^+K^-K_S^0$. In Sec. II, we introduce the formalism used for the DP amplitude analyses. In Sec. III, we briefly describe the *BABAR* detector and data sets used, and Sec. IV describes the event selection and backgrounds. Section V describes the maximum-likelihood (ML) fit parametrization and implementation. In Sec. VI, we present studies of the DP structure in the three modes, which enable us to determine the nominal DP models. In Sec. VII, we then present the final fit results including measurements of CP violation. We discuss systematic uncertainties in Sec. VIII and summarize our results in Sec. IX.

II. DECAY MODEL FORMALISM

Taking advantage of the interference pattern in the DP, we measure the magnitudes and phases of the different resonant decay modes using an unbinned maximum-likelihood fit.

[1]Charge-conjugate decays are implied throughout, unless otherwise indicated.

We consider the decay of a B meson with four-momentum p_B into the three daughters K_1, K_2, and K_3, with corresponding four-momenta p_1, p_2, and p_3. The squares of the invariant masses are given by $s_{ij} = m_{ij}^2 = (p_i + p_j)^2$.

We will use the following convention for the K indices:

(i) For $B^\pm \to K^\pm K^\mp K^\pm$, $K_1 \equiv K^\pm$, $K_2 \equiv K^\mp$, and $K_3 \equiv K^\pm$. The indices for the two like-sign kaons are defined such that $s_{12} \leq s_{23}$.

(ii) For $B^\pm \to K_S^0 K_S^0 K^\pm$, $K_1 \equiv K_S^0$, $K_2 \equiv K_S^0$, and $K_3 \equiv K^\pm$. The indices for the two K_S^0 are defined such that $s_{13} \leq s_{23}$.

(iii) For $\overset{(-)}{B}{}^0 \to K^+ K^- K_S^0$, $K_1 \equiv K^+$, $K_2 \equiv K^-$, and $K_3 \equiv K_S^0$.

The s_{ij} obey the relation

$$s_{12} + s_{13} + s_{23} = m_B^2 + m_{K_1}^2 + m_{K_2}^2 + m_{K_3}^2. \quad (1)$$

The DP distribution of the $B^\pm$ decays is given by

$$\frac{d\Gamma}{ds_{12}ds_{23}} = \frac{1}{(2\pi)^3}\frac{1}{32m_{B^+}^3}|\overset{(-)}{\mathcal{A}}|^2, \quad (2)$$

where $\mathcal{A}$ ($\bar{\mathcal{A}}$) is the Lorentz-invariant amplitude of the B^+ (B^-) three-body decay, and is a function of s_{12} and s_{23}.

For $B^0 \to K^+K^-K_S^0$, the time dependence of the decay rate is a function of DP location. With $\Delta t \equiv t_{\rm sig} - t_{\rm tag}$ defined as the proper time interval between the decay of the fully reconstructed $B^0 \to K^+K^-K_S^0$ ($B^0_{\rm sig}$) and that of the other meson ($B^0_{\rm tag}$) from the $\Upsilon(4S)$, the time-dependent decay rate over the DP is given by

$$\begin{aligned}\frac{d\Gamma}{ds_{12}ds_{23}d\Delta t} = &\frac{1}{(2\pi)^3}\frac{1}{32m_{B^0}^3}\frac{e^{-|\Delta t|/\tau_{B^0}}}{4\tau_{B^0}}\\ &\times[|\mathcal{A}|^2 + |\bar{\mathcal{A}}|^2 - Q(1-2w)(|\mathcal{A}|^2 - |\bar{\mathcal{A}}|^2)\\ &\times\cos\Delta m_d\Delta t + Q(1-2w)\\ &\times 2{\rm Im}[e^{-2i\beta}\bar{\mathcal{A}}\,\mathcal{A}^*]\sin\Delta m_d\Delta t], \end{aligned} \quad (3)$$

where τ_{B^0} is the neutral B meson lifetime and Δm_d is the $B^0 - \bar{B}^0$ mixing frequency. $\mathcal{A}$ ($\bar{\mathcal{A}}$) is the amplitude of the $B^0_{\rm sig}$ ($\bar{B}^0_{\rm sig}$) decay and $Q = +1(-1)$ when the $B^0_{\rm tag}$ is identified as a B^0 ($\bar{B}^0$). The parameter w is the fraction of events in which the $B^0_{\rm tag}$ is tagged with the incorrect flavor.

We describe the distribution of signal events in the DP using an isobar approximation, which models the total amplitude as a coherent sum of amplitudes from N individual decay channels (''isobars''):

$$\overset{(-)}{\mathcal{A}} = \sum_{j=1}^{N}\overset{(-)}{\mathcal{A}}_j, \quad (4)$$

where

$$\mathcal{A}_j \equiv a_j F_j(s_{12}, s_{23}), \qquad \bar{\mathcal{A}}_j \equiv \bar{a}_j \bar{F}_j(s_{12}, s_{23}). \quad (5)$$

The F_j are DP-dependent dynamical amplitudes described below, and a_j are complex coefficients describing the relative magnitude and phase of the different decay channels. All the weak phase dependence is contained in a_j, and F_j contains strong dynamics only.

The amplitudes must be symmetric under exchange of identical bosons, so for $B^+ \to K^+K^-K^+$, $F_j(s_{12}, s_{23})$ is replaced by $F_j(s_{12}, s_{23}) + F_j(s_{23}, s_{12})$. Similarly, in $B^+ \to K_S^0K_S^0K^+$, $F_j(s_{12}, s_{23})$ is replaced by $F_j(s_{12}, s_{23}) + F_j(s_{12}, s_{13})$.

We parametrize the complex coefficients as

$$a_j = c_j(1 + b_j)e^{i(\phi_j + \delta_j)}, \quad \bar{a}_j = c_j(1 - b_j)e^{i(\phi_j - \delta_j)}, \quad (6)$$

where c_j, b_j, ϕ_j, and δ_j are real numbers. We define the fit fraction (FF_j) for an intermediate state as

$$FF_j \equiv \frac{\iint(|\mathcal{A}_j|^2 + |\bar{\mathcal{A}}_j|^2)ds_{12}ds_{23}}{\iint(|\mathcal{A}|^2 + |\bar{\mathcal{A}}|^2)ds_{12}ds_{23}}. \quad (7)$$

Note that the sum of the fit fractions is not necessarily unity, due to interference between states. This interference can be quantified by the interference fit fractions FF_{jk}, defined as

$$FF_{jk} \equiv 2\,{\rm Re}\frac{\iint(\mathcal{A}_j\mathcal{A}_k^* + \bar{\mathcal{A}}_j\bar{\mathcal{A}}_k^*)ds_{12}ds_{23}}{\iint(|\mathcal{A}|^2 + |\bar{\mathcal{A}}|^2)ds_{12}ds_{23}}. \quad (8)$$

With this definition,

$$\sum_j FF_j + \sum_{j<k} FF_{jk} = 1. \quad (9)$$

In the B^+ modes, the direct CP asymmetry $A_{CP}(j)$ for a particular intermediate state is given by

$$A_{CP}(j) \equiv \frac{\iint(|\bar{\mathcal{A}}_j|^2 - |\mathcal{A}_j|^2)ds_{12}ds_{23}}{\iint(|\bar{\mathcal{A}}_j|^2 + |\mathcal{A}_j|^2)ds_{12}ds_{23}} = \frac{-2b_j}{1 + b_j^2}, \quad (10)$$

while there can also be a CP asymmetry in the interference between two intermediate states, which depends on both the b's and δ's of the interfering states. We define the CP-violating phase difference as

$$\Delta\phi_j \equiv \arg(a_j\bar{a}_j^*) = 2\delta_j. \quad (11)$$

For $B^0 \to K^+K^-K_S^0$, we can define the direct CP asymmetry as in Eq. (10), while we can also compute the effective β for an intermediate state as

$$\beta_{{\rm eff},j} \equiv \tfrac{1}{2}\arg(e^{2i\beta}a_j\bar{a}_j^*) = \beta + \delta_j, \quad (12)$$

which quantifies the CP violation due to the interference between mixing and decay.

The resonance dynamics are contained within the F_j terms, which are the product of the invariant mass and angular distributions,

$$F_j^L(s_{12}, s_{23}) = R_j(m)X_L(|\vec{p}^\star|r')X_L(|\vec{q}|r)T_j(L, \vec{p}, \vec{q}), \quad (13)$$

where

(i) L is the spin of the resonance.

(ii) m is the invariant mass of the decay products of the resonance.

(iii) $R_j(m)$ is the resonance mass term or "line shape" (e.g. Breit-Wigner).

(iv) $\vec{p}^{\star}$ is the momentum of the "bachelor" particle, i.e., the particle not belonging to the resonance, evaluated in the rest frame of the B.

(v) $\vec{p}$ and $\vec{q}$ are the momenta of the bachelor particle and one of the resonance daughters, respectively, both evaluated in the rest frame of the resonance. For K^+K^- resonances, $\vec{q}$ is assigned to the momentum of the K^+, except for $B^- \to K^-K^+K^-$ decays, in which case $\vec{q}$ is assigned to the momentum of the K^-. For $K^0_SK^0_S$ resonances, it is irrelevant to which K^0_S we assign $\vec{q}$, so we arbitrarily assign $\vec{q}$ to whichever K^0_S forms the smaller angle with the K^+.

(vi) X_L are Blatt-Weisskopf angular momentum barrier factors [12]:

$$L = 0\text{: } X_L(z) = 1, \tag{14}$$

$$L = 1\text{: } X_L(z) = \sqrt{\frac{1+z_0^2}{1+z^2}}, \tag{15}$$

$$L = 2\text{: } X_L(z) = \sqrt{\frac{9+3z_0^2+z_0^4}{9+3z^2+z^4}}, \tag{16}$$

where z equals $|\vec{q}|r$ or $|\vec{p}^{\star}|r'$, and z_0 is the value of z when the invariant mass of the pair of daughter particles equals the mass of the parent resonance. r and r' are effective meson radii. We take r' as zero, while r is taken to be 4 ± 2.5 $(\mathrm{GeV}/c)^{-1}$ for each resonance.

(vii) $T_j(L, \vec{p}, \vec{q})$ are the Zemach tensors [13], which describe the angular distributions:

$$L = 0\text{: } T_j = 1, \tag{17}$$

$$L = 1\text{: } T_j = 4\vec{p}\cdot\vec{q}, \tag{18}$$

$$L = 2\text{: } T_j = \tfrac{16}{3}[3(\vec{p}\cdot\vec{q})^2 - (|\vec{p}||\vec{q}|)^2]. \tag{19}$$

The helicity angle of a resonance is defined as the angle between $\vec{p}$ and $\vec{q}$, measured in the rest frame of the resonance. For a K_1K_2 resonance, the helicity angle will be called θ_3, and is the angle between K_3 and K_1. In $B^0 \to K^+K^-K^0_S$, because $\vec{q}$ is defined as the K^+ momentum for both B^0 and $\bar{B}^0$ decays, there is a sign flip between B^0 and $\bar{B}^0$ amplitudes for odd-L K^+K^- resonances:

$$\bar{F}_j(s_{12}, s_{23}) = F_j(s_{12}, s_{13}) = (-1)^L F_j(s_{12}, s_{23}). \tag{20}$$

In contrast, for $B^+ \to K^+K^-K^+$ and $B^+ \to K^0_SK^0_SK^+$, $\bar{F}_j(s_{12}, s_{23})$ always equals $F_j(s_{12}, s_{23})$.

For most resonances in this analysis the R_j are taken to be relativistic Breit-Wigner (RBW) [14] line shapes:

$$R_j(m) = \frac{1}{(m_0^2 - m^2) - im_0\Gamma(m)}, \tag{21}$$

where m_0 is the nominal mass of the resonance and $\Gamma(m)$ is the mass-dependent width. In the general case of a spin-L resonance, the latter can be expressed as

$$\Gamma(m) = \Gamma_0\left(\frac{|\vec{q}|}{|\vec{q}_0|}\right)^{2L+1}\left(\frac{m_0}{m}\right)X_L^2(|\vec{q}|r). \tag{22}$$

The symbol Γ_0 denotes the nominal width of the resonance. The values of m_0 and Γ_0 are listed in Table I. The symbol $|\vec{q}_0|$ denotes the value of $|\vec{q}|$ when $m = m_0$.

For the $f_0(980)$ line shape the Flatté form [16] is used. In this case

$$R_j(m) = \frac{1}{(m_0^2 - m^2) - i(g_\pi\rho_{\pi\pi}(m) + g_K\rho_{KK}(m))}, \tag{23}$$

where

$$\rho_{\pi\pi}(m) = \sqrt{1 - 4m^2_{\pi^\pm}/m^2}, \tag{24}$$

$$\rho_{KK}(m) = \sqrt{1 - 4m^2_K/m^2}. \tag{25}$$

Here, m_K is the average of the $K^\pm$ and K^0_S masses, and g_π and g_K are coupling constants for which the values are given in Table I.

In this paper, we test several different models to account for NR $B \to KKK$ decays. *BABAR's* previous analysis [7] of $B^+ \to K^+K^-K^+$ modeled the NR decays with an exponential model given by

$$F_{\mathrm{NR}}(s_{12}, s_{23}) = e^{\alpha s_{12}} + e^{\alpha s_{23}}, \tag{26}$$

TABLE I. Parameters of the DP model used in the fit. Values are given in MeV$(/c^2)$ unless specified otherwise. All parameters are taken from Ref. [14], except for the $f_0(980)$ parameters, which are taken from Ref. [15].

Resonance	Parameters	Line shape
$\phi(1020)$	$m_0 = 1019.455 \pm 0.020$ $\Gamma_0 = 4.26 \pm 0.04$	RBW
$f_0(980)$	$m_0 = 965 \pm 10$ $g_\pi = (0.165 \pm 0.018)\mathrm{GeV}^2/c^4$ $g_K/g_\pi = 4.21 \pm 0.33$	Flatté
$f_0(1500)$	$m_0 = 1505 \pm 6$ $\Gamma_0 = 109 \pm 7$	RBW
$f_0(1710)$	$m_0 = 1720 \pm 6$ $\Gamma_0 = 135 \pm 8$	RBW
$f_2'(1525)$	$m_0 = 1525 \pm 5$ $\Gamma_0 = 73^{+6}_{-5}$	RBW
NR decays		See text
χ_{c0}	$m_0 = 3414.75 \pm 0.31$ $\Gamma_0 = 10.3 \pm 0.6$	RBW

where the symmetrization is explicit. α is a parameter to be determined empirically. This model consists purely of K^+K^- S-wave decays.

The most recently published $B^0 \to K^+K^-K^0_S$ analyses by Belle [9] and *BABAR* [10] both used what we will call an *extended exponential model*. This model adds $K^+K^0_S$ and $K^-K^0_S$ exponential terms:

$$\begin{aligned}\mathcal{A}_{\rm NR}(s_{12}, s_{23}) &= a_{12}e^{\alpha s_{12}} + a_{13}e^{\alpha s_{13}} + a_{23}e^{\alpha s_{23}},\\ \bar{\mathcal{A}}_{\rm NR}(s_{12}, s_{23}) &= a_{12}e^{\alpha s_{12}} + a_{13}e^{\alpha s_{23}} + a_{23}e^{\alpha s_{13}}.\end{aligned} \tag{27}$$

We also test a *polynomial model*, consisting of explicit S-wave and P-wave terms, each of which has a quadratic dependence on m_{12}:

$$\begin{aligned}\mathcal{A}_{\rm NR}(s_{12}, s_{23}) = &(a_{S0} + a_{S1}x + a_{S2}x^2)\\ &+ (a_{P0} + a_{P1}x + a_{P2}x^2)P_1(\cos\theta_3),\end{aligned} \tag{28}$$

where $x \equiv m_{12} - \Omega$, and Ω is an offset that we define as

$$\Omega \equiv \tfrac{1}{2}(m_B + \tfrac{1}{3}(m_{K_1} + m_{K_2} + m_{K_3})), \tag{29}$$

and P_1 is the first Legendre polynomial. In this paper, we normalize the P_ℓ such that

$$\int_{-1}^{1} P_\ell(x)P_k(x)dx = \delta_{\ell k}. \tag{30}$$

Note that in the $B^+ \to K^+K^-K^+$ channel, we symmetrize all terms in Eq. (28):

$$\mathcal{A}_{\rm NR,total} = \mathcal{A}_{\rm NR}(s_{12}, s_{23}) + \mathcal{A}_{\rm NR}(s_{23}, s_{12}). \tag{31}$$

This results in S-wave and P-wave terms for both the (K_1K_2) and (K_2K_3) pairs. In the $B^+ \to K^0_SK^0_SK^+$ channel, the P-wave term is forbidden by Bose-Einstein symmetry.

In Sec. VI, we present studies that allow us to determine the nominal DP model. The components of the nominal model are summarized in Table I. Other components, taken into account only to estimate the systematic uncertainties due to the DP model, are discussed in Sec. VIII.

III. THE *BABAR* DETECTOR AND DATA SET

The data used in this analysis were collected with the *BABAR* detector at the PEP-II asymmetric energy e^+e^- storage rings. The $B^0 \to K^+K^-K^0_S$ and $B^+ \to K^0_SK^0_SK^+$ modes use an integrated luminosity of 429 fb^{-1} or $(471 \pm 3) \times 10^6$ $B\bar{B}$ pairs collected at the $\Upsilon(4S)$ resonance ("on resonance"). The $B^+ \to K^+K^-K^+$ mode uses 426 fb^{-1} or $(467 \pm 5) \times 10^6$ $B\bar{B}$ pairs collected on resonance. We also use approximately 44 fb^{-1} collected 40 MeV below the $\Upsilon(4S)$("off resonance") to study backgrounds.

A detailed description of the *BABAR* detector is given in Ref. [17]. Charged-particle trajectories are measured with a five-layer, double-sided silicon vertex tracker (SVT) and a 40-layer drift chamber (DCH), both operating inside a 1.5-T magnetic field. Charged-particle identification (PID) is achieved by combining information from a ring-imaging Cherenkov device and ionization energy loss (dE/dx) measurements from the DCH and SVT. Photons are detected and their energies measured in a CsI(Tl) electromagnetic calorimeter inside the magnet coil. Muon candidates are identified in the instrumented flux return of the solenoid.

We use GEANT4-based [18] software to simulate the detector response and account for the varying beam and environmental conditions. Using this software, we generate signal and background Monte Carlo (MC) event samples in order to estimate the efficiencies and expected backgrounds.

IV. EVENT SELECTION AND BACKGROUNDS

A. $B^+ \to K^+K^-K^+$

The $B^+ \to K^+K^-K^+$ candidates are reconstructed from three charged tracks that are each consistent with a kaon hypothesis. The PID requirement is about 85% efficient for kaons, with a pion misidentification rate of around 2%. The tracks are required to form a good-quality vertex. Also, the total energy in the event must be less than 20 GeV.

Most backgrounds arise from random track combinations in $e^+e^- \to q\bar{q}(q = u, d, s, c)$ events (hereafter referred to as *continuum* events). These backgrounds peak at $\cos\theta_T = \pm 1$, where θ_T is the angle in the e^+e^- center-of-mass (c.m.) frame between the thrust axis of the B-candidate decay products and the thrust axis of the rest of the event. To reduce these backgrounds, we require $|\cos\theta_T| < 0.95$. Additional continuum suppression is achieved by using a neural network (NN) classifier with five input variables: $|\cos\theta_T|$, $|\cos\theta_B|$, $|\Delta t/\sigma_{\Delta t}|$, $\mathcal{L}_2/\mathcal{L}_0$, and the output of a B-flavor tagging algorithm. Here, θ_B is the angle in the e^+e^- c.m. frame between the B-candidate momentum and the beam axis, Δt is the difference between the decay times of the B^+ and B^- candidates with $\sigma_{\Delta t}$ its uncertainty, and $\mathcal{L}_k = \sum_j |\mathbf{p}_j| P_k(\cos\theta_j)$. The sum includes every track and neutral cluster not used to form the B candidate, and θ_j is the angle in the e^+e^- c.m. frame between the momentum $\mathbf{p}_j$ and the B-candidate thrust axis. P_k is the kth Legendre polynomial. The NN is trained on signal MC events and off-resonance data. We place a requirement on the NN output that removes 65% of continuum events while removing only 6% of signal events.

Further discrimination is achieved with the energy-substituted mass $m_{\rm ES} \equiv \sqrt{(s/2 + \mathbf{p}_i \cdot \mathbf{p}_B)^2/E_i^2 - p_B^2}$ and energy difference $\Delta E \equiv E_B^* - \frac{1}{2}\sqrt{s}$, where $(E_B, \mathbf{p}_B)$ and $(E_i, \mathbf{p}_i)$ are the four-vectors of the B candidate and the initial electron-positron system measured in the laboratory frame, respectively. The asterisk denotes the e^+e^- c.m. frame, and s is the invariant mass squared of the electron-positron system. Signal events peak at the B mass (≈ 5.279 GeV/c^2) for $m_{\rm ES}$, and at zero for ΔE. We require $5.27 < m_{\rm ES} < 5.29$ GeV/c^2 and $|\Delta E| < 0.1$ GeV. An $m_{\rm ES}$

TABLE II. Summary of the $B\bar{B}$ backgrounds in $B^+ \to K^+K^-K^+$. The "Expected yields" column gives the expected number of events for 467×10^6 $B\bar{B}$ pairs, based on MC simulation. The "Fitted yields" column gives the fitted number of events from the best solution of the fit on the data (see Sec. VII A).

Class	Decay	Expected yields	Fitted yields
1	$B^+ \to$ charmless	42 ± 5	Fixed
2	$B^+ \to \bar{D}^{(*)0}X$, $\bar{D}^0 \to K^+K^-$	195 ± 7	170 ± 21
3	$B^+ \to \bar{D}^{(*)0}X$, $\bar{D}^0 \to K^+\pi^-$	117 ± 5	133 ± 34
4	$B^+ \to \bar{D}^0K^+(\bar{D}^0 \to K^+\pi^-)$	92 ± 5	23 ± 9
5	$B^+ \to \bar{D}^0K^+(\bar{D}^0 \to K^+K^-)$	233 ± 13	238 ± 22
6	$B^+ \to J/\psi K^+(J/\psi \to K^+K^-)$	38 ± 5	45 ± 10
7	$B^+B^-/B^0\bar{B}^0$ remaining	386 ± 12	261 ± 56

sideband region with $m_{\rm ES} < 5.27$ GeV$/c^2$ is used for background characterization. After the calculation of $m_{\rm ES}$ and ΔE, we refit each B candidate with the invariant mass of the candidate constrained to agree with the nominal B mass [14], in order to improve the resolution on the DP position and to ensure that Eq. (1) is satisfied. About 8% of signal events have multiple B candidates that pass the selection criteria. If an event has multiple B candidates, we select the one with the best vertex χ^2. To avoid having events that have candidates in both the $m_{\rm ES}$ sideband and in the signal region, the best-candidate selection is performed prior to the $m_{\rm ES}$ and ΔE selection. The overall selection efficiency for $B^+ \to K^+K^-K^+$ is 33%.

We use MC simulation to study backgrounds from B decays ($B\bar{B}$ background). In this paper, we treat $B \to KKK$ decays containing intermediate charm decays as background, except for $B \to \chi_{c0}K(\chi_{c0} \to KK)$, which we treat as signal. Most of the $B\bar{B}$ backgrounds come from $B \to D^{(*)}X$ decays. We study 20 of the most prominent B^+B^- background modes using simulated exclusive samples, and split these modes into six classes, summarized in Table II. These classes have distinct kinematic distributions, and so will be handled separately in the ML fit, as described in Sec. V. Class 1 contains various charmless B^+ decays, the largest of which is $B^+ \to K^+K^-\pi^+$. Class 2 includes a number of decays containing $D^0 \to K^+K^-$ in the decay chain. Class 3 includes various decays containing $\bar{D}^0 \to K^+\pi^-$. Class 4 consists of $B^+ \to \bar{D}^0K^+(\bar{D}^0 \to K^+\pi^-)$ decays. We also include classes for signal-like $B^+ \to K^+K^-K^+$ decays coming from $B^+ \to \bar{D}^0K^+$ (class 5) and $B^+ \to J/\psi K^+$ (class 6). These decays have the same $m_{\rm ES}$ and ΔE distributions as signal, but can be distinguished from charmless signal by their location on the DP. We include a seventh $B\bar{B}$ background class, which contains the remaining inclusive B^+B^- and $B^0\bar{B}^0$ decays.

B. $B^+ \to K^0_SK^0_SK^+$

The $B^+ \to K^0_SK^0_SK^+$ candidates are reconstructed by combining a charged track with two $K^0_S \to \pi^+\pi^-$ candidates. The charged track is required to satisfy a kaon-PID requirement that is about 95% efficient for kaons, with a pion misidentification rate of around 4%. The K^0_S candidates are each required to have a mass within 12 MeV$/c^2$ of the nominal K^0_S mass and a lifetime significance exceeding 3 standard deviations. We also require that $\cos\alpha_{K_S} > 0.999$, where α_{K_S} is the angle between the momentum vector of the K^0_S candidate and the vector connecting the decay vertices of the B^+ and K^0_S candidates in the laboratory frame. The total energy in the event must be less than 20 GeV.

To reduce continuum backgrounds, we require $|\cos\theta_T| < 0.9$. We also use the same NN as for $B^+ \to K^+K^-K^+$, and place a requirement on the NN output that removes 49% of continuum events while removing 4% of signal events. Finally, the B candidates are required to satisfy $5.26 < m_{\rm ES} < 5.29$ GeV$/c^2$ and $|\Delta E| < 0.1$ GeV. An $m_{\rm ES}$ sideband region with $m_{\rm ES} < 5.26$ GeV$/c^2$ is used for background characterization. After the calculation of $m_{\rm ES}$ and ΔE, the B candidates are refitted with a B mass constraint. The overall selection efficiency for $B^+ \to K^0_SK^0_SK^+$ (with both $K^0_S \to \pi^+\pi^-$) is 27%.

About 2% of signal events have multiple B candidates that pass the selection criteria. In such cases, we choose the B candidate whose K^0_S candidates have invariant masses closest to the nominal K^0_S mass. Because there can be multiple B candidates that share one or more of the same kaon candidates, multiple B candidates may still remain after this step. In this case, we select the B candidate whose K^+ candidate has PID information most consistent with the kaon hypothesis. If multiple B candidates still remain, we select the one with the best vertex χ^2. The best candidate selection is performed prior to the $m_{\rm ES}$ and ΔE selection.

$B\bar{B}$ backgrounds are studied with MC events. We study 10 of the most prominent background decay modes using simulated exclusive samples, and group them into three classes, summarized in Table III. Class 1 contains $B^+ \to D^0\pi^+(D^0 \to K^0_SK^0_S)$ and $B^+ \to K^0_SK^{*+}(K^{*+} \to K^0_S\pi^+)$ decays. Class 2 contains various B^+B^- and $B^0\bar{B}^0$ decays, dominated by the charmless decays $B^0 \to K^0_SK^0_SK^0_S$ and $B^0 \to K^{(*)+}K^-K^0_S$. Signal-like $B^+ \to K^0_SK^0_SK^+$ decays coming from $B^+ \to D^0K^+$ make up class 3. The remaining $B\bar{B}$ backgrounds are grouped into a fourth class.

TABLE III. Summary of the $B\bar{B}$ backgrounds in $B^+ \to K^0_S K^0_S K^+$. The "Expected yields" column gives the expected number of events for 471×10^6 $B\bar{B}$ pairs, based on MC simulation. In the maximum-likelihood fit on the data (Sec. VII B), the yield of each class is fixed to its MC expectation.

Class	Decay	Expected yields
1	$B^+ \to \bar{D}^0\pi^+(\bar{D}^0 \to K^0_S K^0_S)$, $B^+ \to K^0_S K^{*+}(K^{*+} \to K^0_S\pi^+)$	6.1 ± 1.2
2	$B^+/B^0 \to$ charmless	23 ± 5
3	$B^+ \to \bar{D}^0 K^+(\bar{D}^0 \to K^0_S K^0_S)$	8.1 ± 1.6
4	$B^+B^-/B^0\bar{B}^0$ remaining	118 ± 6

C. $B^0 \to K^+K^-K^0_S$

$B^0 \to K^+K^-K^0_S$ candidates are reconstructed by combining two charged tracks with a K^0_S candidate. The charged tracks are required to be consistent with a kaon hypothesis. For most events, we apply tight kaon-PID requirements that are about 90% efficient for kaons with a pion misidentification rate of around 1.5%. Looser PID requirements ($\sim$95% efficient, $\sim$6% pion misidentification) are applied in the $m_{12} < 1.1$ GeV/c^2 region, to increase the signal efficiency for $B^0 \to \phi K^0_S$. K^0_S candidates are reconstructed in both the $K^0_S \to \pi^+\pi^-$ and $K^0_S \to \pi^0\pi^0$ decay modes. $K^0_S \to \pi^+\pi^-$ candidates are required to have a mass within 20 MeV/c^2 of the nominal K^0_S mass, while $K^0_S \to \pi^0\pi^0$ candidates are required to have a mass $m_{\pi^0\pi^0}$ in the range $(m_{K^0_S} - 20\ \text{MeV}/c^2) < m_{\pi^0\pi^0} < (m_{K^0_S} + 30\ \text{MeV}/c^2)$, where $m_{K^0_S}$ is the nominal K^0_S mass. Both $K^0_S \to \pi^+\pi^-$ and $K^0_S \to \pi^0\pi^0$ candidates are required to have a lifetime significance of at least 3 standard deviations, and to satisfy $\cos\alpha_{K_S} > 0.999$. The π^0 candidates are formed from two photon candidates, with each photon required to have a laboratory energy greater than 50 MeV and a transverse shower profile consistent with an electromagnetic shower.

We reduce continuum backgrounds by requiring $|\cos\theta_T| < 0.9$. In addition, we use a NN containing the variables $|\cos\theta_T|$, $|\cos\theta_B|$, and $\mathcal{L}_2/\mathcal{L}_0$. Since we are performing a time-dependent analysis of $B^0 \to K^+K^-K^0_S$, we omit $|\Delta t/\sigma_{\Delta t}|$ from the NN in order not to bias the fit. We train the NN on signal MC events and off-resonance data. We make a requirement on the NN output that removes 26% of continuum events in the $K^0_S \to \pi^+\pi^-$ channel, and 24% of continuum events in the $K^0_S \to \pi^0\pi^0$ channel, with only a 2% loss of signal events. B candidates must satisfy $5.26 < m_{\rm ES} < 5.29$ GeV/c^2 and $-0.06(-0.12) < \Delta E < 0.06$ GeV for $K^0_S \to \pi^+\pi^-$ ($K^0_S \to \pi^0\pi^0$). An $m_{\rm ES}$ sideband region with $m_{\rm ES} < 5.26$ GeV/c^2 is used for background characterization. After the calculation of $m_{\rm ES}$ and ΔE, the B candidates are refitted with a B mass constraint. The overall selection efficiency for $B^0 \to K^+K^-K^0_S$ is 31% for $K^0_S \to \pi^+\pi^-$ and 7% for $K^0_S \to \pi^0\pi^0$.

The time difference Δt is obtained from the measured distance along the beam direction between the positions of the $B^0_{\rm sig}$ and $B^0_{\rm tag}$ decay vertices, using the boost $\beta\gamma = 0.56$ of the e^+e^- system. We require that B candidates have $|\Delta t| < 20$ ps and an uncertainty on Δt less than 2.5 ps. To determine the flavor of $B^0_{\rm tag}$ we use the B flavor tagging algorithm of Ref. [1], which produces six mutually exclusive tagging categories. We also retain untagged events (about 23% of signal events) in a seventh category, since these events contribute to the measurements of the branching fractions, although not to the *CP* asymmetries.

Multiple B candidates pass the selection criteria in about 4% of $K^0_S \to \pi^+\pi^-$ signal events and 11% of $K^0_S \to \pi^0\pi^0$ signal events. If an event has multiple candidates, we choose the B candidate using criteria similar to those used for $B^+ \to K^0_S K^0_S K^+$. The best candidate selection is performed prior to the $m_{\rm ES}$, ΔE, and Δt selection.

$B\bar{B}$ backgrounds are studied with MC events and grouped into five classes, summarized in Table IV. We include classes for signal-like $B^0 \to K^+K^-K^0_S$ decays coming from $B^0 \to D^-K^+$ (class 1), $D^-_s K^+$ (class 2), $\bar{D}^0 K^0_S$ (class 3), and $J/\psi K^0_S$ (class 4). The remaining $B\bar{B}$ backgrounds are grouped into a fifth class.

V. THE MAXIMUM-LIKELIHOOD FIT

We perform an unbinned extended maximum-likelihood fit [19] to measure the inclusive $B \to KKK$ event yields and the resonant amplitudes and *CP*-violating parameters.

TABLE IV. Summary of the $B\bar{B}$ backgrounds in $B^0 \to K^+K^-K^0_S$. The "Expected yields" columns give the expected number of events for 471×10^6 $B\bar{B}$ pairs, based on MC simulation. The "Fitted yields" columns give the fitted number of events from the best solution of the fit on the data (see Sec. VII C).

Class	Decay	Expected yields		Fitted yields	
		$K^0_S \to \pi^+\pi^-$	$K^0_S \to \pi^0\pi^0$	$K^0_S \to \pi^+\pi^-$	$K^0_S \to \pi^0\pi^0$
1	$B^0 \to D^-K^+(D^- \to K^-K^0_S)$	42 ± 13	4 ± 1	36 ± 7	3.6 ± 0.6
2	$B^0 \to D^-_s K^+(D^-_s \to K^-K^0_S)$	33 ± 6	3 ± 1	11 ± 4	1.1 ± 0.4
3	$B^0 \to \bar{D}^0 K^0_S(\bar{D}^0 \to K^+K^-)$	10 ± 1	1.0 ± 0.1	16 ± 5	1.9 ± 0.5
4	$B^0 \to J/\psi K^0_S(J/\psi \to K^+K^-)$	10 ± 1	1.0 ± 0.1	4 ± 4	0.5 ± 0.4
5	$B^+B^-/B^0\bar{B}^0$ remaining	141 ± 7	123 ± 6	29 ± 28	48 ± 18

TABLE V. Definition of parameters in the event PDF for B^+ decays shown in Eq. (32). The $B\bar{B}$ background classes are given in Tables II and III.

Parameter	Definition
$N_{\rm sig}$	Total fitted $B \to KKK$ signal yield in the data sample
$N_{q\bar{q}}$	Fitted continuum yield
Q_i	Charge of the B candidate, $+1$ or -1
$A_{q\bar{q}}$	Charge asymmetry in continuum events
$N^{B\bar{B}}_{\rm class}$	Number of $B\bar{B}$-related background classes considered in the fit
$N_{B\bar{B}j}$	Fitted or fixed yield in $B\bar{B}$ background class j
$A_{B\bar{B}j}$	Charge asymmetry in $B\bar{B}$ background class j

The fit uses the variables $m_{\rm ES}$, ΔE, NN, m_{12}, and m_{23} to discriminate signal from background. Events with both charges or tag flavors Q are simultaneously included in the fits in order to measure CP violation. For $B^0 \to K^+K^-K^0_S$, the additional variable Δt enables the determination of mixing-induced CP violation.

The selected on-resonance data sample is assumed to consist of signal, continuum background, and B background components.

A. The likelihood function

1. $B^+ \to K^+K^-K^+$ and $B^+ \to K^0_SK^0_SK^+$

The probability density function (PDF) $\mathcal{P}_i$ for an event i is the sum of the probability densities of all event components (signal, $q\bar{q}$ continuum background, $B\bar{B}$ background), namely

$$\mathcal{P}_i \equiv N_{\rm sig}\mathcal{P}_{{\rm sig},i} + N_{q\bar{q}}\frac{1}{2}(1 - Q_iA_{q\bar{q}})\mathcal{P}_{q\bar{q},i} + \sum_{j=1}^{N^{B\bar{B}}_{\rm class}} N_{B\bar{B}j}\frac{1}{2}(1 - Q_iA_{B\bar{B}j})\mathcal{P}_{B\bar{B}j,i}. \quad (32)$$

The parameters are defined in Table V.

The PDFs $\mathcal{P}_{X,i}$ have the general form

$$\mathcal{P}_{X,i} \equiv P_{X,i}(m_{\rm ES})P_{X,i}(\Delta E)P_{X,i}({\rm NN}, s_{12}, s_{23})P_{X,i}(s_{12}, s_{23}, Q). \quad (33)$$

This form neglects some small correlations between observables. Biases due to correlations in the signal PDF are assessed using MC events passed through a GEANT4-based detector simulation (see Sec. VIII).

The extended likelihood function is given by

$$\mathcal{L} \propto e^{-\bar{N}}\prod_i^N \mathcal{P}_i, \quad (34)$$

where N is the number of events entering into the fit, and

$$\bar{N} \equiv N_{\rm sig} + N_{q\bar{q}} + \sum_{j=1}^{N^{B\bar{B}}_{\rm class}} N_{B\bar{B}j}$$

is the total fitted number of events.

A total of 43 parameters are allowed to vary in the $B^+ \to K^+K^-K^+$ fit. They include eight yields (signal, continuum, and six $B\bar{B}$ background yields) and 30 parameters for the complex amplitudes a_j from Eq. (5) (see Table VII in Sec. VII). The last five parameters are $A_{q\bar{q}}$, one parameter each for the continuum $m_{\rm ES}$ and ΔE PDFs, and the means of the signal $m_{\rm ES}$ and ΔE PDFs (see Sec. V C). The $A_{B\bar{B}j}$ are fixed to their MC expectations, except for classes 5 and 6, in which they are fixed to the world average [14] and 0, respectively.

A total of 41 parameters are allowed to vary in the $B^+ \to K^0_SK^0_SK^+$ fit. They include two yields (signal and continuum) and 16 parameters for the complex amplitudes a_j (see Table IX in Sec. VII). The last 23 parameters are $A_{q\bar{q}}$, one parameter each for the shapes of the continuum $m_{\rm ES}$ and ΔE PDFs, the means of the signal $m_{\rm ES}$ and ΔE PDFs, and 18 parameters for the continuum NN PDFs (nine h_{0i} and nine g_i; see Sec. V C). The $A_{B\bar{B}j}$ are fixed to their MC

TABLE VI. Definition of parameters in the event PDF for B^0 decays shown in Eq. (35). The $B\bar{B}$ background classes are described in Table IV.

Parameter	Definition
$N_{\rm sig}$	Total fitted $B \to KKK$ signal yield in the data sample, including $B\bar{B}$ background classes 1–4
f^c	Fraction of events that are tagged in category c, with $\sum_c f^c = 1$ This fraction is assumed to be the same for signal and $B\bar{B}$ background events
$N^c_{q\bar{q}}$	Fitted continuum yield in tagging category c
Q_i	Tag flavor of the event, defined to be $+1$ for a $B^0_{\rm tag}$ and -1 for a $\bar{B}^0_{\rm tag}$
$N_{B\bar{B}}$	Fitted yield in $B\bar{B}$ background class 5

TABLE VII. Isobar parameters [defined in Eq. (6)] for $B^+ \to K^+K^-K^+$, solutions I and II. The same b and δ parameters are used for the $f_0(1500)$, $f_2'(1525)$, and $f_0(1710)$, and we choose to quote their fitted values in the $f_2'(1525)$ rows. The NR coefficients are defined in Eq. (28). Phases are given in degrees. Only statistical uncertainties are given.

Parameter		Solution I	Solution II
$\phi(1020)K^\pm$	c	0.0311 ± 0.0043	0.043 ± 0.009
	ϕ	177 ± 13	-53 ± 13
	b	-0.064 ± 0.022	-0.037 ± 0.022
	δ	11 ± 7	-10 ± 6
$f_0(980)K^\pm$	c	1.64 ± 0.23	1.5 ± 0.5
	ϕ	118 ± 12	-34 ± 11
	b	0.040 ± 0.041	-0.32 ± 0.11
	δ	4.5 ± 3.3	-12 ± 7
$f_0(1500)K^\pm$	c	0.179 ± 0.031	0.28 ± 0.07
	ϕ	-45 ± 11	-41 ± 15
$f_2'(1525)K^\pm$	c	0.00130 ± 0.00022	0.00160 ± 0.00038
	ϕ	34 ± 10	43 ± 16
	b	-0.07 ± 0.05	-0.09 ± 0.05
	δ	-0.8 ± 2.8	0.5 ± 2.6
$f_0(1710)K^\pm$	c	0.254 ± 0.044	0.32 ± 0.08
	ϕ	44 ± 9	45 ± 16
$\chi_{c0}K^\pm$	c	0.114 ± 0.017	0.170 ± 0.038
	ϕ	9 ± 12	31 ± 15
	δ	-2 ± 6	-2 ± 6
NR			
	b	-0.030 ± 0.022	-0.062 ± 0.024
a_{S0}	c	1.0 (fixed)	1.0 (fixed)
	ϕ	0 (fixed)	0 (fixed)
a_{S1}	c	2.09 ± 0.38	0.4 ± 1.2
	ϕ	160 ± 14	1 ± 162
a_{S2}	c	0.33 ± 0.08	0.45 ± 0.35
	ϕ	157 ± 12	-65 ± 19
a_{P0}	c	1.6 ± 0.5	2.3 ± 1.9
	ϕ	7 ± 20	130 ± 25
a_{P1}	c	0.80 ± 0.07	0.85 ± 0.30
	ϕ	-159 ± 6	-114 ± 12
a_{P2}	c	0.49 ± 0.15	0.77 ± 0.38
	ϕ	-110 ± 17	-60 ± 18

expectations, except for class 3, which is fixed to the world average [14].

2. $B^0 \to K^+K^-K^0_S$

For this decay we use a similar unbinned maximum-likelihood fit to that described in Sec. V A 1, but there are some significant differences. The components in the fit may be separated by the flavor and tagging category of the tag-side B decay.

The probability density function $\mathcal{P}_i^c$ for an event i in tagging category c [1] is the sum of the probability densities of all components, namely

$$\mathcal{P}_i^c \equiv N_{\rm sig} f^c \mathcal{P}^c_{{\rm sig},i} + N^c_{q\bar{q}} \mathcal{P}^c_{q\bar{q},i} + N_{B\bar{B}} f^c \mathcal{P}^c_{B\bar{B},i}. \quad (35)$$

The parameters are defined in Table VI. The signal PDF includes components for the $B\bar{B}$ background classes 1–4 listed in Table IV, since they lead to the same $K^+K^-K^0_S$ final state. The PDFs $\mathcal{P}^c_{X,i}$ are the products of PDFs for one or more variables,

$$\mathcal{P}^c_{X,i} \equiv P^c_{X,i}(m_{\rm ES}) P^c_{X,i}(\Delta E) P^c_{X,i}({\rm NN}, s_{12}, s_{23}) \times P^c_{X,i}(s_{12}, s_{23}, \Delta t, \sigma_{\Delta t}, Q), \quad (36)$$

where i is the event index. Not all the PDFs depend on the tagging category; the general notations $P^c_{X,i}$ and $\mathcal{P}^c_{X,i}$ are used for simplicity.

The extended likelihood function evaluated for events in all tagging categories is given by

$$\mathcal{L} \equiv \prod_{c=1}^{7} e^{-\bar{N}^c} \prod_i^{N^c} \mathcal{P}_i^c, \quad (37)$$

where N^c is the number of events entering into the fit in category c, and $\bar{N}^c \equiv N_{\rm sig} f^c + N^c_{q\bar{q}} + N_{B\bar{B}} f^c$ is the total fitted number of events in category c.

The maximum-likelihood fit is performed simultaneously over both the $K^0_S \to \pi^+\pi^-$ and $K^0_S \to \pi^0\pi^0$ modes. The signal isobar model parameters are constrained to be equal for both modes, but otherwise the PDFs may differ.

A total of 90 parameters are allowed to vary in the fit. They include the 18 inclusive yields (for both $K^0_S \to \pi^+\pi^-$ and $K^0_S \to \pi^0\pi^0$, there are nine yields: signal, $B\bar{B}$, and seven continuum yields, one per tagging category). We also allow 32 parameters for the complex amplitudes a_j to vary (22 are shown in Table XI, six are b and δ parameters corresponding to the parameters in Table XIII, and four describe the background classes 1–4 in Table IV, which we model as noninterfering isobars). The remaining 40 parameters include 38 parameters that describe the continuum PDF shapes (one ΔE parameter and 18 NN parameters, for both $K^0_S \to \pi^+\pi^-$ and $K^0_S \to \pi^0\pi^0$), as well as the means of the signal $m_{\rm ES}$ and ΔE PDFs for $K^0_S \to \pi^+\pi^-$ only (see Sec. V C).

B. The Dalitz plot and Δt PDFs

For $B^+ \to K^+K^-K^+$ and $B^+ \to K^0_S K^0_S K^+$, the signal DP PDFs are given by

$$P_{\rm sig}(s_{12}, s_{23}, Q) = d\Gamma(s_{12}, s_{23}, Q)\varepsilon(s_{12}, s_{23}), \quad (38)$$

where $d\Gamma$ is defined in Eq. (2), and ε is the DP-dependent selection efficiency, determined from MC simulation. We assume equal efficiencies for B^+ and B^- events, and consider a possible asymmetry as a systematic uncertainty.

For $B^0 \to K^+K^-K^0_S$, the time- and DP-dependent signal PDF is given by

$$P^c_{\rm sig}(s_{12}, s_{23}, \Delta t, \sigma_{\Delta t}, Q) = d\Gamma(s_{12}, s_{23}, \Delta t, Q)\varepsilon(s_{12}, s_{23}) \otimes \mathcal{R}(\Delta t, \sigma_{\Delta t}), \quad (39)$$

where $d\Gamma$ is defined in Eq. (3) and the Δt resolution function is a sum of three Gaussian distributions. The parameters of the Δt resolution function and the tagging-category-dependent mistag rate are determined by a fit to fully reconstructed B^0 decays [1].

To account for finite resolution on DP location, the signal PDFs are convolved with a 2×2-dimensional resolution function

$$\mathcal{R}\,(s^r_{12}, s^r_{23}, s^t_{12}, s^t_{23}), \tag{40}$$

which represents the probability for an event with true DP coordinates (s^t_{12}, s^t_{23}) to be reconstructed with coordinates (s^r_{12}, s^r_{23}). It obeys the unitarity condition

$$\iint \mathcal{R}(s^r_{12}, s^r_{23}, s^t_{12}, s^t_{23}) ds^r_{12} ds^r_{23} = 1 \quad \forall\ s^t_{12}, s^t_{23}. \tag{41}$$

The $\mathcal{R}$ function is obtained from MC simulation.

For $B^+ \to K^+K^-K^+$ and $B^+ \to K^0_S K^0_S K^+$, the $B\bar{B}$ background DP PDFs are histograms obtained from MC samples. The histograms have variable bin sizes calculated using an adaptive binning method to ensure that fine binning is used where the DP distributions have narrow structures.

For $B^0 \to K^+K^-K^0_S$, the generic $B\bar{B}$ background DP PDFs are likewise histograms obtained from MC samples. The background classes 1–4 given in Table IV, however, are modeled as noninterfering isobars, and so their DP and time dependence is included in Eq. (39).

The DP PDFs for continuum events are described by histograms similar to those for $B\bar{B}$ backgrounds. The PDFs are modeled with data taken from $m_{\rm ES}$ sidebands, with a correction applied for $B\bar{B}$ backgrounds present in the sidebands.

For $B^0 \to K^+K^-K^0_S$, the Δt distribution of the continuum events is modeled with the sum of an exponential decay and prompt component, convolved with a double-Gaussian resolution function. The parameters are taken from a fit to data in the $m_{\rm ES}$ sideband. The Δt distribution of the generic $B\bar{B}$ backgrounds is modeled in the same way, but the parameters are taken from a fit to MC samples. In the nominal fit, we assume zero CP violation in the backgrounds, but as a systematic we include CP violation in the $B\bar{B}$ exponential decay component.

C. PDFs of other fit variables

The $m_{\rm ES}$ and ΔE distributions of signal events are described by modified Gaussians of the form

$$P(x) \propto \exp\left[-\frac{(x-x_0)^2}{2\sigma^2_{\pm} + \alpha_{\pm}(x-x_0)^2}\right], \tag{42}$$

where σ_+ and α_+ are used when $x > x_0$, and σ_- and α_- when $x < x_0$. Most parameters are taken from fits to signal MC events. The means x_0 are allowed to vary in the nominal fits to data, except for the $B^0 \to K^+K^-K^0_S$, $K^0_S \to \pi^0\pi^0$ channel.

The $m_{\rm ES}$ distributions for continuum events are modeled with a threshold function [20], while the ΔE distributions are modeled with first-order polynomials. The $m_{\rm ES}$ and ΔE shape parameters are allowed to vary in the nominal fits.

A variety of PDFs are used to describe the $m_{\rm ES}$ and ΔE distributions of the various $B\bar{B}$ background categories. The PDF shapes for each category are taken from MC simulation. Those $B\bar{B}$ backgrounds that have the same true final state as signal events are modeled with the same $m_{\rm ES}$, ΔE, and NN PDFs as signal events.

The output of the NN does not have an easily parametrized shape, so we split the distribution into ten bins, with the bin size chosen so that approximately equal numbers of signal events are expected in each bin; continuum events peak at larger values of the bin number. The binned NN is then easily described using histogram PDFs. The PDFs for signal and $B\bar{B}$ background events are taken from fits to MC events. In the case of $B^+ \to K^+K^-K^+$, due to the large number of signal events, we obtain the histogram bin heights for signal from a separate fit to data, and then fix these parameters in the nominal fit. For continuum events, the NN output is correlated with the distance from the center of the DP. To account for this correlation, the continuum NN PDF is given by a histogram with bin heights h_i equal to $h_{0i} + g_i\Delta_{\rm DP}$. Here, $\Delta_{\rm DP}$ is the smallest of (m_{12}, m_{23}, m_{13}).

D. Fitting method

The ML fits are performed with MINUIT [21]. Proper normalization of the DP PDFs poses a technical challenge in these fits, because some of the resonance amplitudes vary rapidly as functions of the DP. The normalization of these PDFs is performed using a numerical 2-dimensional integration algorithm that makes use of adaptive binning [22]. The speed of this algorithm allows the masses and decay widths of resonances to be varied in the fit. The normalization of the DP PDFs is recalculated at each step in the fit for which these parameters are varied.

VI. DETERMINATION OF DALITZ MODEL

The Dalitz plots for the three $B \to KKK$ modes are shown in Fig. 1. Before fitting A_{CP} parameters, we first decide which resonances and NR terms to include in the DP model for each of the $B \to KKK$ modes. Because the $B^+ \to K^+K^-K^+$ mode has the largest number of events, we primarily use it to guide our decision making, but the other modes are useful as well. The studies in this section are performed in a "CP-blind" fashion, which means that we constrain the CP-violating parameters of the signal and background components to zero, except in the case of $B^0 \to K^+K^-K^0_S$, where we constrain $\beta_{\rm eff}$ to β for all isobars.

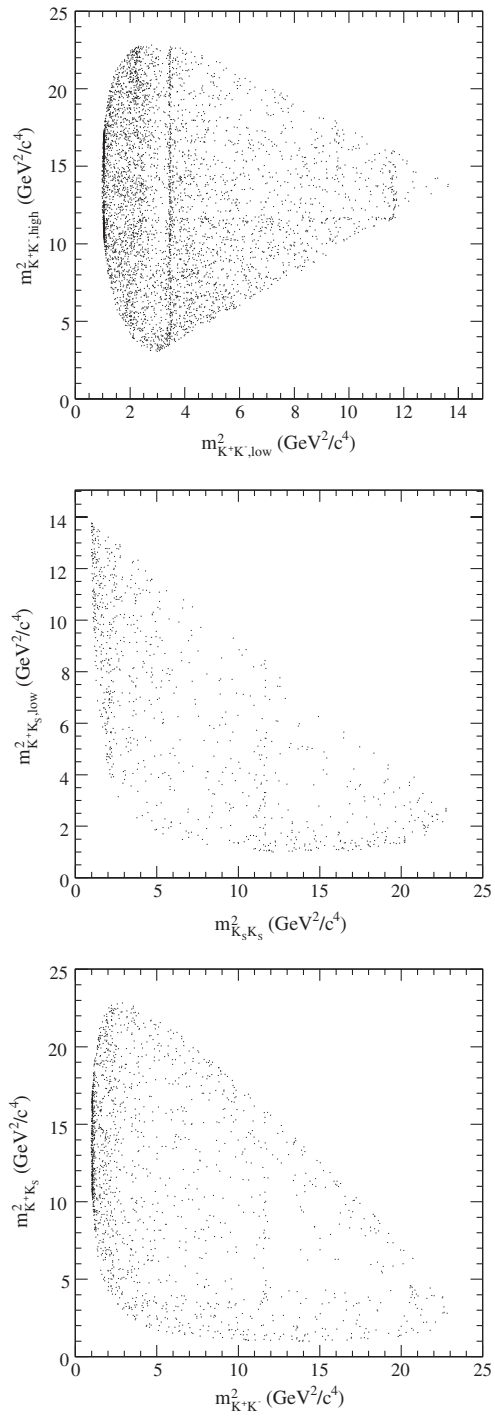

FIG. 1. Dalitz plots for $B^+ \to K^+K^-K^+$ (top panel), $B^+ \to K^0_S K^0_S K^+$ (middle panel), and $B^0 \to K^+K^-K^0_S$ (bottom panel). Points correspond to candidates in data that pass the full event selection, with an additional requirement that the NN output be 7 or less, in order to enhance the signal.

One important goal is to understand the nature of the so-called $f_X(1500)$ resonance seen in several previous analyses. Both *BABAR* [7,10] and Belle [8,9] have modeled this resonance as a scalar particle, but while *BABAR* has found its mass and width to be inconsistent with any established resonance, Belle has found a mass and width consistent with the $f_0(1500)$. There is also confusion surrounding the branching fraction to $f_X(1500)K$. Belle's $B^+ \to K^+K^-K^+$ and $B^0 \to K^+K^-K^0_S$ analyses both find multiple solutions for the fit fraction for f_X. Some solutions favor a small fit fraction, less than 10%, while others favor a large fit fraction, greater than 50%. *BABAR* obtained a small fit fraction in $B^0 \to K^+K^-K^0_S$, but a large fit fraction in $B^+ \to K^+K^-K^+$. A large, broad structure around $m_{K^+K^-} = 1500$ MeV$/c^2$ is also seen by *BABAR* in $B^+ \to K^+K^-\pi^+$ [23] but not in $B^+ \to K^0_S K^0_S \pi^+$ [24]. *BABAR's* analysis of $B^0 \to K^0_S K^0_S K^0_S$ [11] does not provide evidence for the $f_X(1500)$.

A. $B^+ \to K^+K^-K^+$

We initially perform a fit to $B^+ \to K^+K^-K^+$ using the same DP model as *BABAR's* previous analysis of this mode, which includes the resonances $\phi(1020)$, $f_0(980)$, $f_X(1500)$, $f_0(1710)$, and χ_{c0}, and an exponential NR model [Eq. (26)]. We allow the NR parameter α, as well as the mass and width of the $f_X(1500)$, to vary in the fit. The $f_X(1500)$ is taken to have a spin of zero. We refer to this hereafter as $B^+ \to K^+K^-K^+$ model A. We find fit parameters consistent with *BABAR's* previous analysis.

To see how well the fit model describes the DP distribution, we calculate angular moments, defined as

$$\langle P_\ell(\cos\theta_3)\rangle \equiv \int_{-1}^{1} d\Gamma P_\ell(\cos\theta_3) d\cos\theta_3, \qquad (43)$$

where θ_3 is the helicity angle between K_3 and K_1, measured in the rest frame of K_1K_2, P_ℓ is the ℓth Legendre polynomial, and the differential decay rate $d\Gamma$ is given in Eq. (2). Note that the angular moments are functions of m_{12} but we suppress this dependence in our notation. Angular moments plotted as a function of m_{12} are an excellent tool for visualizing the agreement between the fit model and data, as they provide more information than ordinary DP projections, in particular, spin information.

If we assume that no K_1K_2 partial waves of a higher order than D wave contribute, and we temporarily ignore the effects of symmetrization, then we can express the overall decay amplitude as a sum of S-wave, P-wave, and D-wave terms:

$$\mathcal{A}(m_{12}, \cos\theta_3) = \mathcal{A}_S P_0(\cos\theta_3) + \mathcal{A}_P e^{i\phi_P} P_1(\cos\theta_3) + \mathcal{A}_D e^{i\phi_D} P_2(\cos\theta_3), \qquad (44)$$

where $\mathcal{A}_k$ and ϕ_k are real-valued functions of m_{12}, and we have factored out the S-wave phase. We can then calculate the angular moments:

$$\langle P_0\rangle = \frac{\mathcal{A}_S^2 + \mathcal{A}_P^2 + \mathcal{A}_D^2}{\sqrt{2}}, \qquad \langle P_1\rangle = \sqrt{2}\mathcal{A}_S\mathcal{A}_P\cos\phi_P + \frac{2\sqrt{10}}{5}\mathcal{A}_P\mathcal{A}_D\cos(\phi_P - \phi_D),$$
$$\langle P_2\rangle = \sqrt{\frac{2}{5}}\mathcal{A}_P^2 + \frac{\sqrt{10}}{7}\mathcal{A}_D^2 + \sqrt{2}\mathcal{A}_S\mathcal{A}_D\cos\phi_D, \qquad \langle P_3\rangle = \frac{3}{5}\sqrt{\frac{30}{7}}\mathcal{A}_P\mathcal{A}_D\cos(\phi_P - \phi_D), \qquad \langle P_4\rangle = \frac{\sqrt{18}}{7}\mathcal{A}_D^2. \tag{45}$$

The symmetrization of the $B^+ \to K^+K^-K^+$ amplitude spoils the validity of Eq. (45). Nevertheless, the angular moments can be calculated both for signal-weighted data and for the fit model, providing a useful tool for checking how well the isobar model describes the data. In Fig. 2, we show angular moments for data compared to the fit model, in the region of the DP above the $\phi(1020)$. The data are signal weighted using the ${}_s\mathcal{P}lot$ [25] technique. The fit model histograms are made by simulating large numbers of events based on the fit results. In Fig. 3, we show the angular moments in the $\phi(1020)$ region.

The angular moments, in particular $\langle P_2\rangle$, show that model A does not describe the data well in the $f_X(1500)$ region. If we replace the $f_X(1500)$ with the $f_0(1500)$ and

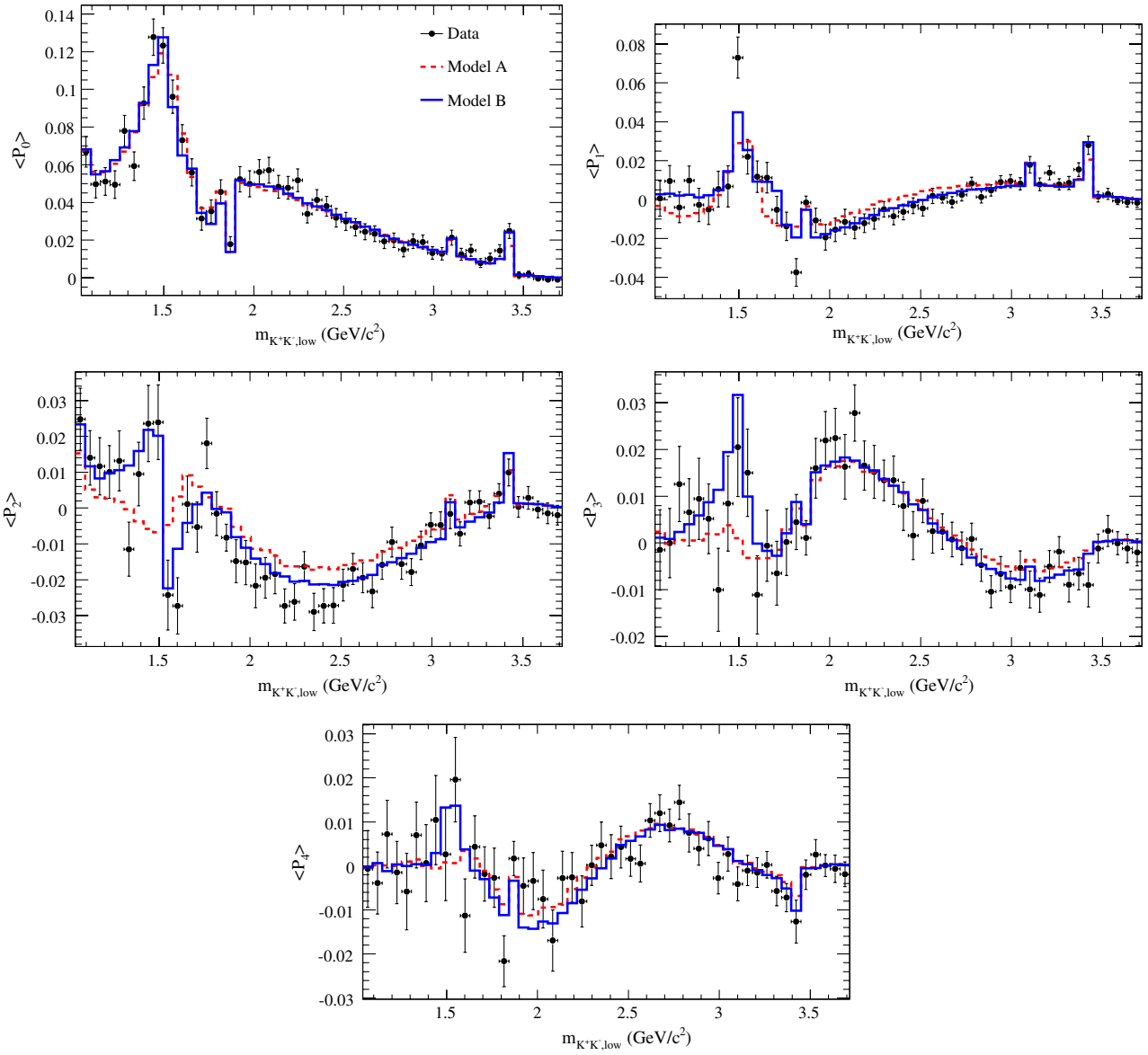

FIG. 2 (color online). $B^+ \to K^+K^-K^+$ angular moments in the region $m_{12} > 1.04$ GeV$/c^2$, computed for signal-weighted data, compared to model A (dashed lines) and model B (solid lines). The signal weighting is performed using the ${}_s\mathcal{P}$lot method. Events with $m_{K^+K^-}$ near the D^0 mass are vetoed.

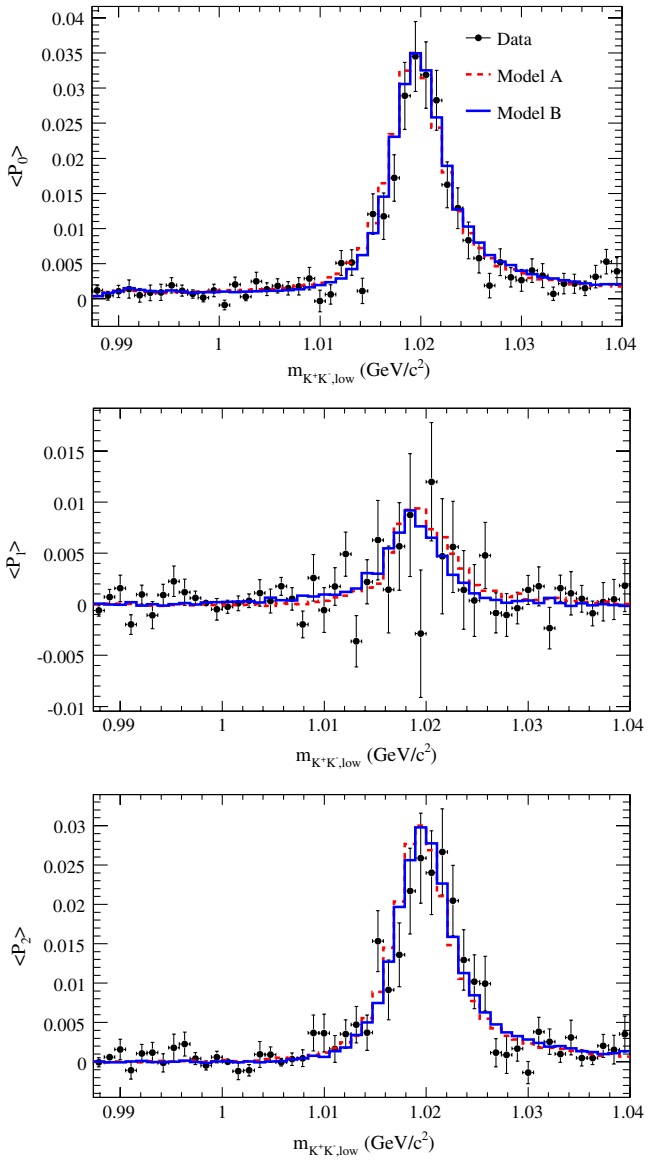

FIG. 3 (color online). $B^+ \to K^+K^-K^+$ angular moments in the region $m_{12} < 1.04$ GeV/c^2, computed for signal-weighted data, compared to model A (dashed lines) and model B (solid lines). The signal weighting is performed using the ${}_s\mathcal{P}$lot method.

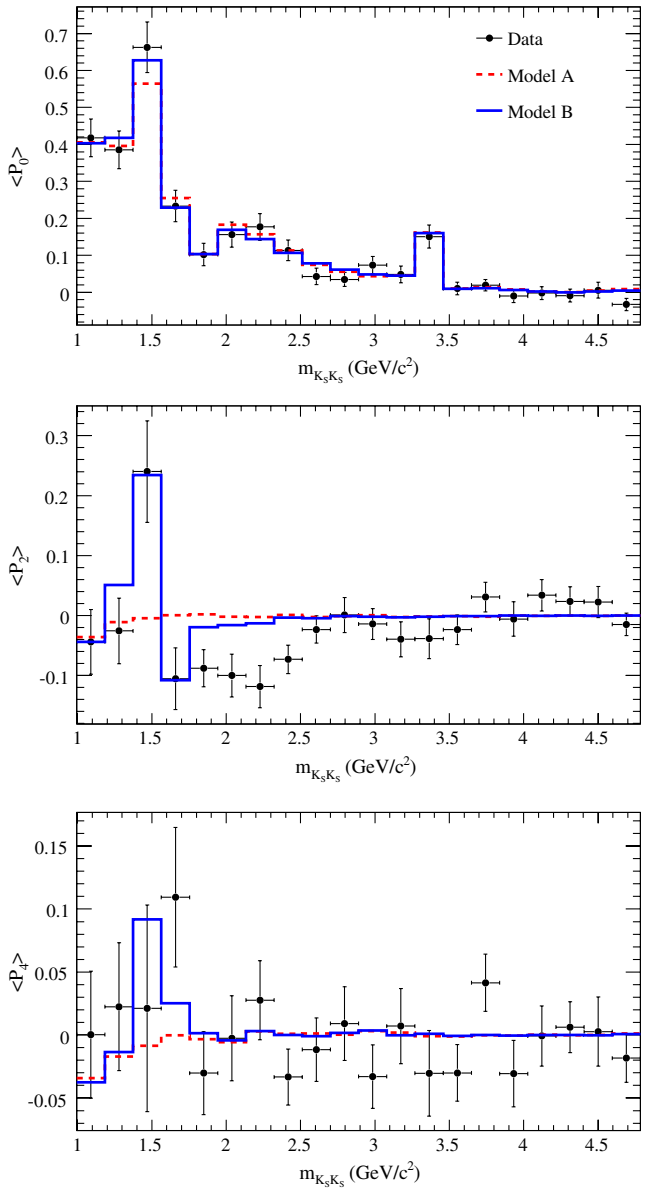

FIG. 4 (color online). $B^+ \to K^0_S K^0_S K^+$ angular moments computed for signal-weighted data, compared to model A (dashed lines) and model B (solid lines). The signal weighting is performed using the ${}_s\mathcal{P}$lot method. Events with $m_{K^0_S K^0_S}$ near the D^0 mass are vetoed.

the $f_2'(1525)$, there is an improvement in $2\ln\mathcal{L}$ of 17 units. As we will discuss shortly, this replacement is also motivated by a peak in $\langle P_2\rangle$ seen in $B^+ \to K^0_S K^0_S K^+$.

We also vary the NR model. The exponential NR model is not very flexible; it assumes no phase motion and only an S-wave term. We fit with a polynomial model [Eq. (28)] instead, which contains S-wave and P-wave terms and allows for phase motion. There is an improvement in $2\ln\mathcal{L}$ of 233 units. However, the polynomial model has 9 more degrees of freedom than the exponential model. We refer to this model [which replaces the $f_X(1500)$ with the $f_0(1500)$ and the $f_2'(1525)$, and which uses the polynomial NR model] hereafter as model B for $B^+ \to K^+K^-K^+$. We compare the angular moments for model B to data in Figs. 2 and 3. Model B matches the data significantly better than model A, especially for $\langle P_1\rangle$ and $\langle P_2\rangle$.

B. $B^+ \to K^0_S K^0_S K^+$

Next we examine $B^+ \to K^0_S K^0_S K^+$, initially including the resonances $f_0(980)$, $f_X(1500)$, $f_0(1710)$, and χ_{c0}. We take the $f_X(1500)$ mass and width from the $B^+ \to K^+K^-K^+$ model A result. We also include a polynomial NR model, but without the P-wave term, which is forbidden. We call this model A for $B^+ \to K^0_S K^0_S K^+$.

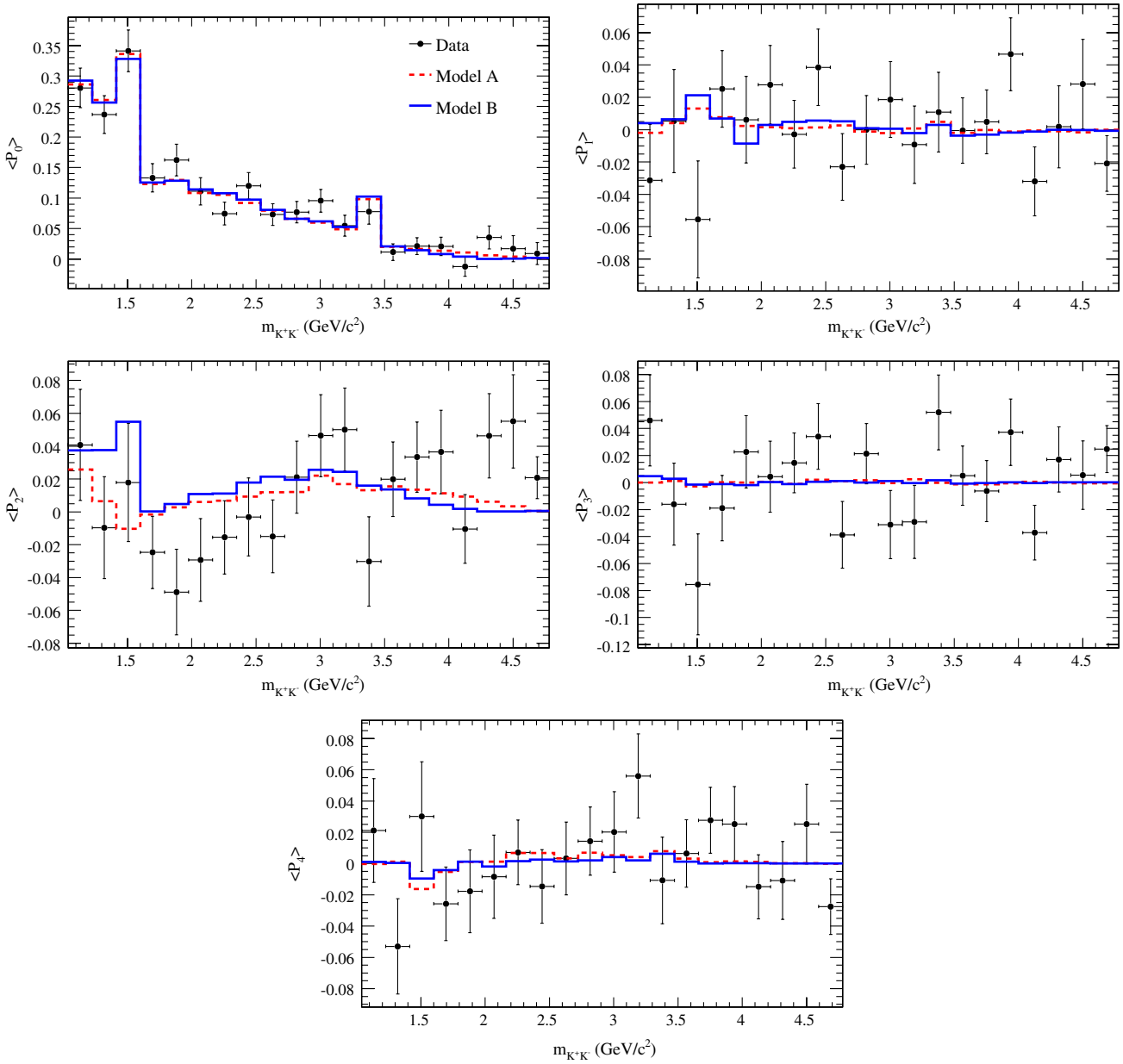

FIG. 5 (color online). $B^0 \to K^+K^-K^0_S$ angular moments in the region $m_{12} > 1.04$ GeV/c^2, computed for signal-weighted data, compared to model A (dashed lines) and model B (solid lines). The signal weighting is performed using the ${}_s\mathcal{P}$lot method. The plots are made using the $K^0_S \to \pi^+\pi^-$ mode only. Events with $m_{K^\pm K^0_S}$ near the D^+ or D^+_s mass are vetoed.

In Fig. 4, we show the angular moments for this model, compared to signal-weighted data. Assuming there are no higher-order $K^0_SK^0_S$ partial waves than D wave, Eq. (45) is valid for $B^+ \to K^0_SK^0_SK^+$. However, because odd partial waves are forbidden in this channel, the odd angular moments are automatically zero. The peak in $\langle P_2\rangle$ around 1.5 GeV/c^2 in Fig. 4 suggests the presence of a tensor resonance. We replace the $f_X(1500)$ with the $f_0(1500)$ and $f'_2(1525)$, and call this model B for $B^+ \to K^0_SK^0_SK^+$. Model B improves $2\ln\mathcal{L}$ by 37 units over model A. The angular moments for model B are shown in Fig. 4. Neither model does a good job of describing $\langle P_2\rangle$ in the region $1.8 < m_{12} < 2.5$ GeV/c^2. As an alternative, we use the model from *BABAR's* $B^0 \to K^0_SK^0_SK^0_S$ analysis [11], which includes $f_0(980)$, $f_0(1710)$, $f_2(2010)$, χ_{c0}, and an exponential NR model like in Eq. (26), except without the second term. For this model, $2\ln\mathcal{L}$ is 52 units worse than for model B. We then add the $f'_2(1525)$ to this model, but its $2\ln\mathcal{L}$ is still 19 units worse than model B. Adding the $f_2(2010)$ or $f_2(2300)$ resonance to model B significantly improves $2\ln\mathcal{L}$ and improves the modeling of the $\langle P_2\rangle$ distribution, but no evidence for these resonances is seen in $B^+ \to K^+K^-K^+$, which has a much higher signal yield. Therefore, we do not include either of these resonances in

our model. We will, however, include these resonances as part of our evaluation of systematic uncertainties.

C. $B^0 \to K^+K^-K^0_S$

Lastly, we examine $B^0 \to K^+K^-K^0_S$. We initially fit with the same model used in *BABAR's* previous analysis, which includes the resonances $\phi(1020)$, $f_0(980)$, $f_X(1500)$, $f_0(1710)$, and χ_{c0}, and the extended exponential NR model given in Eq. (27). We take the mass and width of the $f_X(1500)$ from the $B^+ \to K^+K^-K^+$ model A result. We hereafter refer to this model as model A for $B^0 \to K^+K^-K^0_S$. Belle's most recent $B^0 \to K^+K^-K^0_S$ analysis uses this same model, although with a different mass and width for the $f_X(1500)$.

Using model A, we obtain fit results consistent with *BABAR's* previous measurement. In Fig. 5, we show the angular moments for this model compared to data. The angular moments in $B^0 \to K^+K^-K^0_S$ are complicated due to the relative minus sign between B^0 and $\bar{B}^0$ amplitudes for odd-L resonances [Eq. (20)]. To account for this, when computing the odd angular moments, we weight the events by $-Q$, where Q is the flavor of the $B^0_{\rm tag}$. Then, Eq. (45) is valid for $B^0 \to K^+K^-K^0_S$, except that for the odd angular moments, the right-hand side must be multiplied by $(1-2w)/((\Delta m_d \tau_{B^0})^2+1)$, which is a dilution factor caused by mistagging and B^0-$\bar{B}^0$ mixing.

We replace the $f_X(1500)$ by the $f_0(1500)$, $f'_2(1525)$, and $f_0(1710)$, and this improves $2\ln\mathcal{L}$ by 18 units. We then replace the NR model with a polynomial NR model containing S-wave and P-wave terms. This improves $2\ln\mathcal{L}$ by an additional 13 units. We refer to this model as model B for $B^0 \to K^+K^-K^0_S$; its angular moments are shown in Fig. 5. The improvement of model B over model A is not evident by examining the angular moments by eye, but model B provides a considerably better likelihood.

D. Conclusion

For each of the three decay modes, model B produces a better fit to the data than model A, at the cost of more free parameters. Model B also eliminates the need for the hypothetical $f_X(1500)$ state. The NR parametrization used in model B greatly improves the fit likelihood in $B^+ \to K^+K^-K^+$, and its large number of parameters make it very flexible. A benefit of this flexibility is that the fit results are then less dependent on the particular choice of NR parametrization. Model B also has a similar form in all three modes (the only difference is the absence of P-wave states in $B^+ \to K^0_S K^0_S K^+$), aiding comparison of results between the modes. In addition to the studies already mentioned, we tested for the presence of the $f_0(1370)$, $f_2(1270)$, $f_2(2010)$, and $f_2(2300)$ in each mode, and in $B^+ \to K^+K^-K^+$ and $B^0 \to K^+K^-K^0_S$, we tested for the $\phi(1680)$. We did not find evidence for any of these resonances. We also tested for the following isospin-1 resonances: $a^0_0(1450)$ in each of the three modes, and $a^\pm_0(980)$ and $a^\pm_0(1450)$ in $B^+ \to K^0_S K^0_S K^+$ and $B^0 \to K^+K^-K^0_S$ only. We did not find evidence for any of these resonances. We henceforth use model B as the nominal fit model for each mode, and only include these additional resonances to evaluate systematic uncertainties.

VII. RESULTS

A. $B^+ \to K^+K^-K^+$

The maximum-likelihood fit of 12 240 candidates results in yields of 5269 ± 84 signal events, 6016 ± 91 continuum events, and 912 ± 54 $B\bar{B}$ events, where the uncertainties are statistical only.

In order to limit the number of fit parameters and improve fit stability, we constrain the A_{CP} and $\Delta\phi$ of the $f_0(1500)$, $f'_2(1525)$, and $f_0(1710)$ to be equal in the fit [i.e., the b and δ parameters, defined in Eq. (6), are constrained to be the same for these isobars]. We also constrain the A_{CP} and $\Delta\phi$ of the S-wave and P-wave NR terms to be equal. Since the A_{CP} in $B^+ \to c\bar{c}K^+$ decays is known to be small [14], we fix the A_{CP} of the χ_{c0} to 0 in the fit. Only *relative* values of c, ϕ, and $\Delta\phi$ are measurable, so as references we fix $c=1$ and $\phi=0$ for the NR term a_{S0} and $\Delta\phi=0$ for all NR terms.

When the fit is repeated starting from input parameter values randomly chosen within wide ranges above and

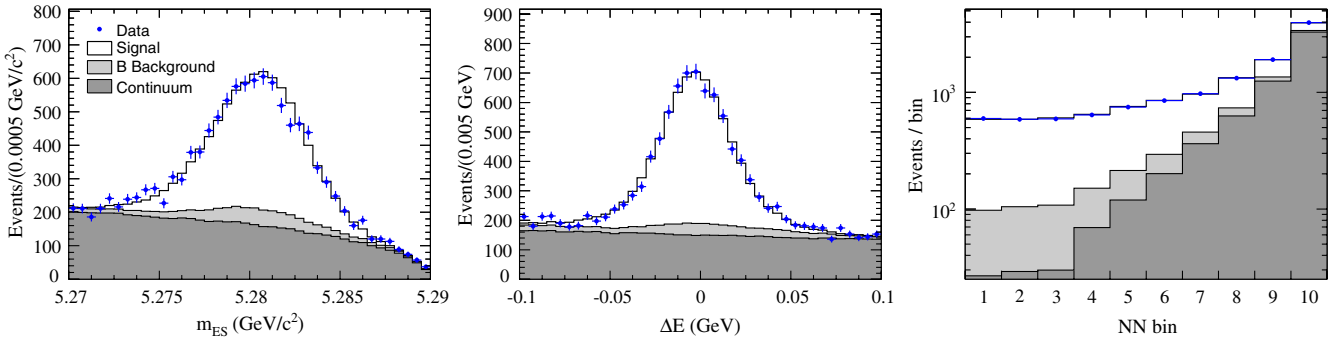

FIG. 6 (color online). Distributions of $m_{\rm ES}$ (left panel), ΔE (center panel), and NN output (right panel) for $B^+ \to K^+K^-K^+$. The NN output is shown in vertical log scale.

below the nominal values for the magnitudes and within the [0°–360°] interval for the phases, we observe convergence toward two solutions with minimum values of the negative log likelihood function $-2\ln\mathcal{L}$ that are separated by 5.6 units. We will refer to them as solution I (the global minimum) and solution II (a local minimum). The two solutions have nearly identical values for most parameters, but differ greatly for some of the isobar parameters. The isobar parameters for both solutions are given in Table VII. The correlation matrices of the isobar parameters are given in Ref. [26].

Figure 6 shows distributions of $m_{\rm ES}$, ΔE and the NN output. Figure 7 shows the m_{12}, m_{23}, and m_{13} distributions for signal- and background-weighted events, using the ${}_s\mathcal{P}lot$ [25] technique.

The fit result for solution I is summarized in Table VIII. The systematic uncertainties are described in Sec. VIII. We report branching fractions for individual decay channels by multiplying the inclusive branching fraction by the fit fractions. This neglects interference between decay channels. The inclusive branching fraction is computed as

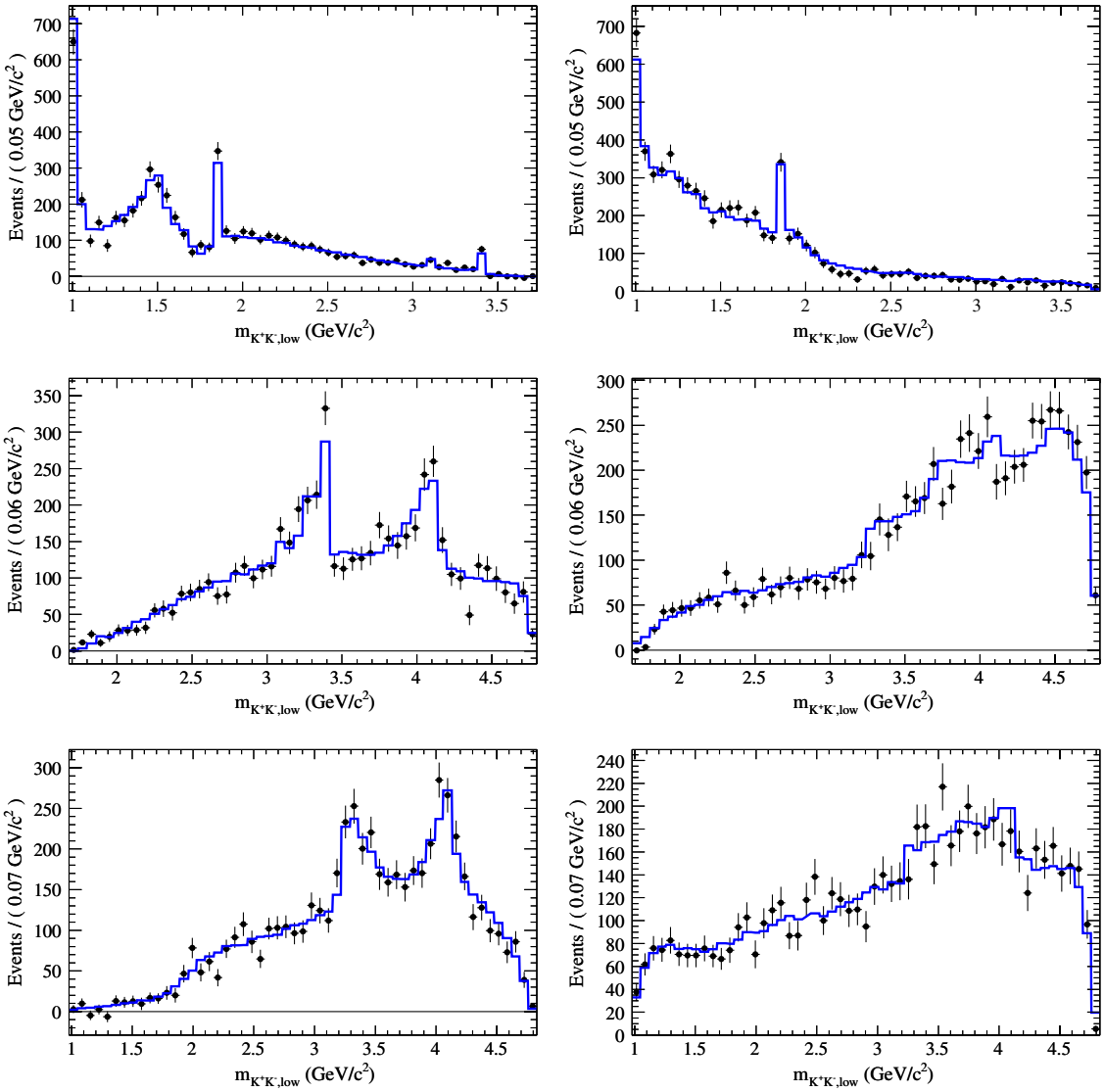

FIG. 7 (color online). Distributions of $m_{12} = m_{K^+K^-,\rm low}$, $m_{23} = m_{K^+K^-,\rm high}$, and $m_{13} = m_{K^+K^+}$, for signal-weighted (left column) and background-weighted (right column) $B^+ \to K^+K^-K^+$ candidates in data. The event weighting is performed using the ${}_s\mathcal{P}$lot method. The fit model (histograms) is shown superimposed over data (points). The signal includes the signal-like $B\bar{B}$ backgrounds (classes 5 and 6 in Table II). The four main peaks in the upper signal plot are, from left to right: the $\phi(1020)$, $f_0(1500)/f_2'(1525)$, D^0 (background), and χ_{c0}. The hornlike peaks in the middle and lower signal plots are reflections from the $\phi(1020)$. The χ_{c0} is also visible around 3.4 GeV/c^2 in the middle signal plot. The upper background plot has a $\phi(1020)$ peak (mainly due to continuum) and D^0 peak (mainly due to $B\bar{B}$).

TABLE VIII. Branching fractions (neglecting interference), *CP* asymmetries, and *CP*-violating phases [see Eq. (11)] for $B^+ \to K^+K^-K^+$. The $\mathcal{B}(B^+ \to RK^+)$ column gives the branching fractions to intermediate resonant states, corrected for secondary branching fractions obtained from Ref. [14]. Central values and uncertainties are obtained from solution I. In addition to quoting the overall NR branching fraction, we quote the *S*-wave and *P*-wave NR branching fractions separately.

Decay mode	$\mathcal{B}(B^+ \to K^+K^-K^+) \times FF_j(10^{-6})$	$\mathcal{B}(B^+ \to RK^+)(10^{-6})$	A_{CP} (%)	$\Delta\phi_j$ (deg)
$\phi(1020)K^+$	$4.48 \pm 0.22^{+0.33}_{-0.24}$	$9.2 \pm 0.4^{+0.7}_{-0.5}$	$12.8 \pm 4.4 \pm 1.3$	$23 \pm 13^{+4}_{-5}$
$f_0(980)K^+$	$9.4 \pm 1.6 \pm 2.8$		$-8 \pm 8 \pm 4$	$9 \pm 7 \pm 6$
$f_0(1500)K^+$	$0.74 \pm 0.18 \pm 0.52$	$17 \pm 4 \pm 12$		
$f_2'(1525)K^+$	$0.69 \pm 0.16 \pm 0.13$	$1.56 \pm 0.36 \pm 0.30$	$14 \pm 10 \pm 4$	$-2 \pm 6 \pm 3$
$f_0(1710)K^+$	$1.12 \pm 0.25 \pm 0.50$			
$\chi_{c0}K^+$	$1.12 \pm 0.15 \pm 0.06$	$184 \pm 25 \pm 14$		$-4 \pm 13 \pm 2$
NR	$22.8 \pm 2.7 \pm 7.6$		$6.0 \pm 4.4 \pm 1.9$	0 (fixed)
NR (*S* wave)	$52^{+23}_{-14} \pm 27$			
NR (*P* wave)	$24^{+22}_{-12} \pm 27$			

$$\mathcal{B}(B^+ \to K^+K^-K^+) = \frac{N_{\rm sig}}{\bar{\varepsilon} N_{B\bar{B}}}, \tag{46}$$

where $N_{B\bar{B}}$ is the total number of $B\bar{B}$ pairs and $\bar{\varepsilon}$ is the average efficiency, estimated by weighting MC events by the measured DP distribution, $|\mathcal{A}|^2 + |\bar{\mathcal{A}}|^2$. We assume equal number of B^+B^- and $B^0\bar{B}^0$ pairs from the $\Upsilon(4S)$. We find $\mathcal{B}(B^+ \to K^+K^-K^+) = (34.6 \pm 0.6 \pm 0.9) \times 10^{-6}$, including the $\chi_{c0}K^+$ channel. We find an inclusive charmless branching fraction (excluding $\chi_{c0}K^+$) of $\mathcal{B}(B^+ \to K^+K^-K^+) = (33.4 \pm 0.5 \pm 0.9) \times 10^{-6}$.

Fit fraction matrices giving the values of FF_{jk} for solutions I and II are shown in the Appendix. Solution I has large destructive interference between the *S*-wave and *P*-wave NR decays. Solution II has a smaller $f_0(980)$ fit fraction and large destructive interference between the $f_0(980)$ and nonresonant decays. We also calculate an overall charmless A_{CP} by integrating the charmless $|\mathcal{A}|^2$ and $|\bar{\mathcal{A}}|^2$ over the DP. We find the charmless $A_{CP}(B^+ \to K^+K^-K^+) = (-1.7^{+1.9}_{-1.4} \pm 1.4)\%$. There is negligible difference between solutions I and II for this quantity.

We plot the signal-weighted m_{12} distribution separately for B^+ and B^- events in Fig. 8. Solutions I and II yield $A_{CP}(\phi(1020)) = (12.8 \pm 4.4)\%$ and $(7.4 \pm 4.5)\%$, respectively, where the uncertainties are statistical only. We perform a likelihood scan in $A_{CP}(\phi(1020))$, shown in Fig. 9. At each scan point, many fits are performed with random initial parameters, and the fit with the largest likelihood is chosen. Thus, the likelihood scan properly accounts for any local minima. The A_{CP} is found to differ from 0 at the 2.8 standard deviation level (2.9σ if one uses only the statistical uncertainties).

Solution II exhibits a very large A_{CP} for the $f_0(980)K^+$ channel, but in solution I this A_{CP} is consistent with 0. A likelihood scan in $A_{CP}(f_0(980))$ is shown in Fig. 10, in which the two solutions are clearly visible.

B. $B^+ \to K^0_S K^0_S K^+$

The maximum-likelihood fit of 3012 candidates results in yields of 636 ± 28 signal events and 2234 ± 50 continuum events, where the uncertainties are statistical only. The $B\bar{B}$ yields are fixed to the expected number of events (Table III), for a total of 155 events.

In order to limit the number of fit parameters, we constrain the A_{CP} and $\Delta\phi$ of every charmless isobar to be equal in the fit. We fix A_{CP} for $\chi_{c0}K^+$ to 0, but leave the

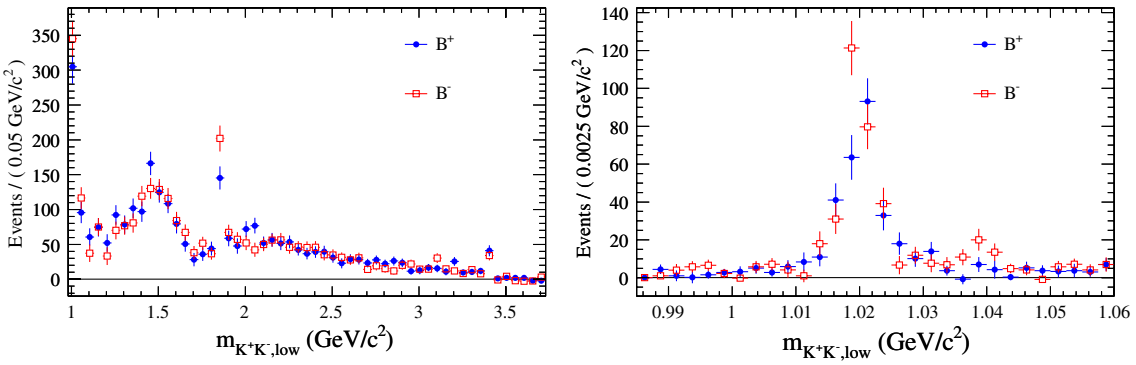

FIG. 8 (color online). Signal-weighted m_{12} distribution for $B^+ \to K^+K^-K^+$ candidates in data, plotted separately for B^+ and B^- events, for the entire DP range (left panel), and the $\phi(1020)$-region only (right panel). The event weighting is performed using the ${}_s\mathcal{P}$lot method. Signal includes irreducible $B\bar{B}$ backgrounds (classes 5 and 6 in Table II).

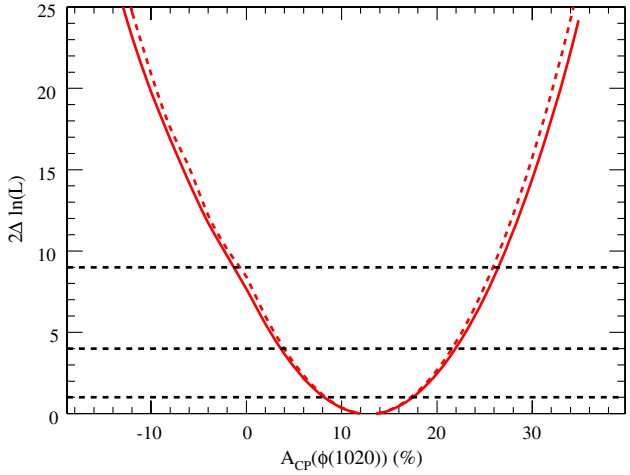

FIG. 9 (color online). Scan of $2\Delta \ln\mathcal{L}$, with (solid line) and without (dashed line) systematic uncertainties, as a function of $A_{CP}(\phi(1020))$ in $B^+ \to K^+K^-K^+$.

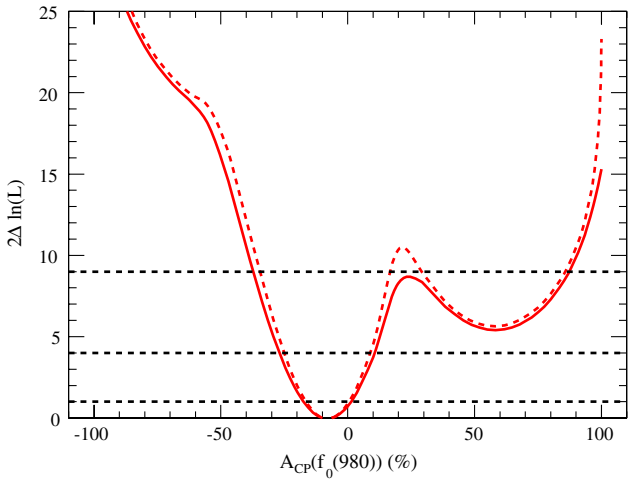

FIG. 10 (color online). Scan of $2\Delta \ln\mathcal{L}$, with (solid line) and without (dashed line) systematic uncertainties, as a function of $A_{CP}(f_0(980))$ in $B^+ \to K^+K^-K^+$.

corresponding $\Delta\phi$ parameter free to vary in the fit. Recalling that only relative values of $\Delta\phi$ are measurable, our choice is therefore to measure the difference between $\Delta\phi$ for the χ_{c0} and the reference $\Delta\phi$ shared by all the other isobars.

Many fits are performed with randomly chosen starting values for the isobar parameters. In addition to the global minimum, 14 other local minima are found with values of $-2\ln\mathcal{L}$ within 9 units (3σ) of the global minimum. These different solutions vary greatly in their isobar parameters, but have consistent signal yields and values of A_{CP}.

Figure 11 shows the distributions of $m_{\rm ES}$, ΔE, and the NN output, compared to the fit model. Figure 12 shows the m_{12}, m_{23}, and m_{13} distributions for signal- and background-weighted events, using the ${}_s\mathcal{P}lot$ technique. We plot the signal-weighted m_{12} distribution separately for B^+ and B^- events in Fig. 13.

The fit result for the global minimum solution is summarized in Tables IX and X. The fit fraction matrix for the global mininum is given in the Appendix, and the correlation matrix of the isobar parameters is given in Ref. [26]. The other minima all have consistent values for the $f_2'(1525)$ and χ_{c0} fit fractions, but wide variations in the fit fractions for the other states are seen. In particular, the fit fraction of the $f_0(980)$ varies between 69% and 152% and the fit fraction of the $f_0(1500)$ varies between 3% and 73%. This means the branching fractions of these states are very poorly constrained with the current data. However, the signal yields for the different solutions only vary between 636 and 640 events. We find a total inclusive branching fraction of $\mathcal{B}(B^+ \to K^0_S K^0_S K^+) = (10.6 \pm 0.5 \pm 0.3) \times 10^{-6}$, or $\mathcal{B}(B^+ \to K^0_S K^0_S K^+) = (10.1 \pm 0.5 \pm 0.3) \times 10^{-6}$ if the χ_{c0} is excluded.

The global minimum has values of $A_{CP} = (4 \pm 5 \pm 2)\%$ and $\Delta\phi = (-25 \pm 65 \pm 11)^\circ$. The A_{CP} for the other minima are between 2% and 4%. A likelihood scan of A_{CP} is shown in Fig. 14. From the likelihood scan, we determine $A_{CP} = (4^{+4}_{-5} \pm 2)\%$.

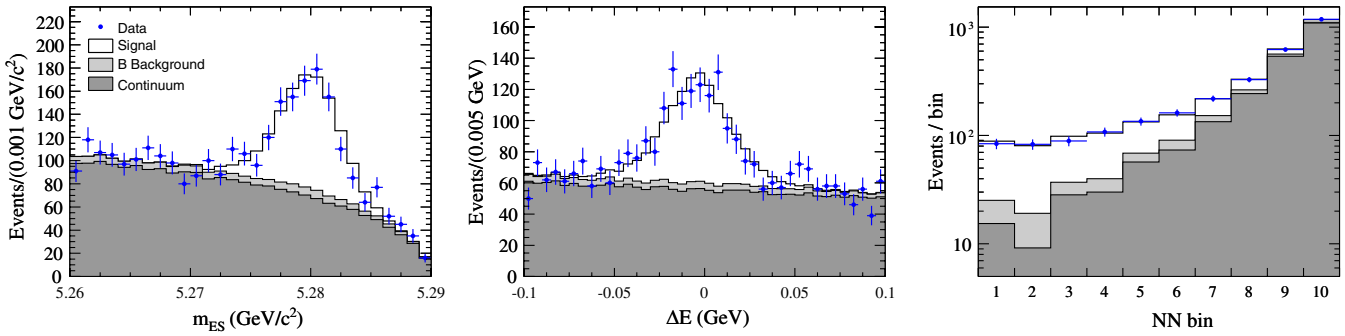

FIG. 11 (color online). Distributions of $m_{\rm ES}$ (left panel), ΔE (center panel), and NN output (right panel) for $B^+ \to K^0_S K^0_S K^+$. The NN output is shown in vertical log scale.

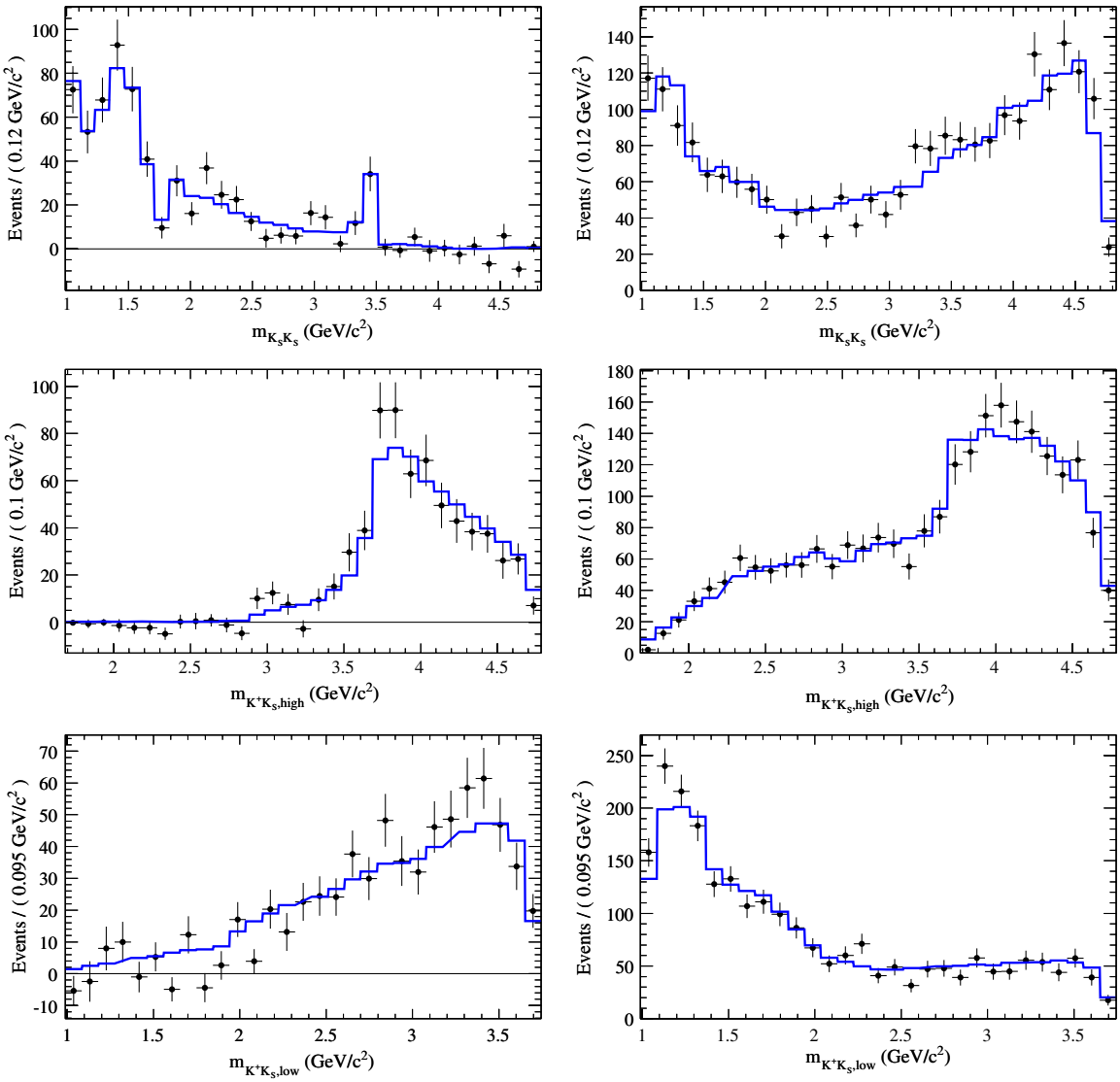

FIG. 12 (color online). Distributions of $m_{12} = m_{K^0_SK^0_S}$, $m_{23} = m_{K^+K^0_S,\mathrm{high}}$, and $m_{13} = m_{K^+K^0_S,\mathrm{low}}$, for signal-weighted (left column) and background-weighted (right column) $B^+ \to K^0_SK^0_SK^+$ candidates in data. The event weighting is performed using the ${}_s\mathcal{P}$lot method. The fit model (histograms) is shown superimposed over data (points). The two main peaks in the upper signal plot are the $f_0(1500)/f_2'(1525)$ and χ_{c0}.

C. $B^0 \to K^+K^-K^0_S$

The maximum-likelihood fit is performed simultaneously to 5627 candidates in the $K^0_S \to \pi^+\pi^-$ channel and 2910 candidates in the $K^0_S \to \pi^0\pi^0$ channel. In the $K^0_S \to \pi^+\pi^-$ channel, we find 1419 ± 43 signal events (including 68 ± 9 signal-like $B\bar{B}$ background events, corresponding to categories 1–4 in Table IV). We also find 4178 ± 71 continuum events and 29 ± 28 remaining $B\bar{B}$ events.

In the $K^0_S \to \pi^0\pi^0$ channel, we find yields of 160 ± 17 signal events (including 7 ± 1 signal-like $B\bar{B}$ background events), 2703 ± 55 continuum events, and 48 ± 18 remaining $B\bar{B}$ events. All uncertainties are statistical only.

We vary three sets of β_{eff} and A_{CP} values in the fit: one for the $\phi(1020)$, another for the $f_0(980)$, and a third that is shared by all the other charmless isobars in order to reduce the number of fit parameters. Note that this last set of isobars contains both even-spin and odd-spin (P-wave NR) terms. Because of the sign flip in Eq. (20), the $\sin\Delta m_d\Delta t$-dependent CP asymmetry [see Eq. (3)] has opposite sign for the even-spin and odd-spin components. We fix the β_{eff} of the χ_{c0} to the SM value, and we fix its $A_{CP}(= -C)$ to 0.

We perform hundreds of fits, each one with randomly chosen starting values for the isobar parameters. In addition to the global minimum, four other local minima are found with values of $-2\ln\mathcal{L}$ within 9 units of the global minimum. These different solutions all have consistent signal yields, but vary greatly for some isobar parameters.

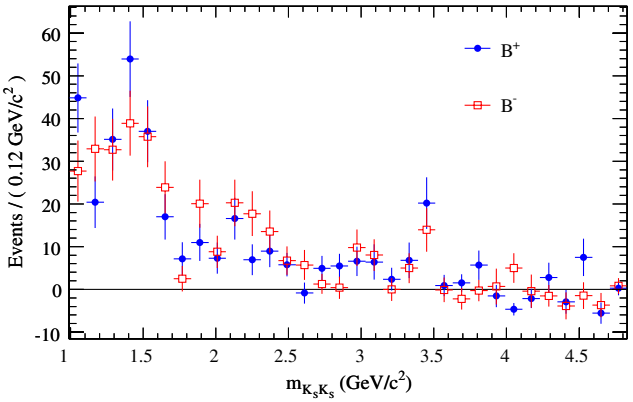

FIG. 13 (color online). Signal-weighted m_{12} distribution for $B^+ \to K^0_S K^0_S K^+$ candidates in data, plotted separately for B^+ and B^- events. The event weighting is performed using the ${}_s\mathcal{P}$lot method. Signal includes irreducible $B\bar{B}$ backgrounds (class 4 in Table III).

Figure 15 shows distributions of $m_{\rm ES}$, ΔE, and the NN output for the $K^0_S \to \pi^+\pi^-$ mode, and Fig. 16 shows the same distributions for the $K^0_S \to \pi^0\pi^0$ mode. Figure 17 shows the m_{12}, m_{23}, and m_{13} distributions for signal- and background-weighted events, for the $K^0_S \to \pi^+\pi^-$ channel only. Figure 18 shows the Δt distribution and the time-dependent asymmetry for signal-weighted events, both for the $\phi(1020)$ region ($1.01 < m_{12} < 1.03$ GeV/c^2) and the $\phi(1020)$-excluded region.

TABLE IX. Isobar parameters for $B^+ \to K^0_S K^0_S K^+$, for the global minimum. The NR coefficients are defined in Eq. (28). Phases are given in degrees. Only statistical uncertainties are given.

Parameter		Value
$f_0(980)K^\pm$	c	3.35 ± 0.22
	ϕ	31 ± 9
$f_0(1500)K^\pm$	c	0.20 ± 0.05
	ϕ	-83 ± 18
$f'_2(1525)K^\pm$	c	$0.001\,79 \pm 0.000\,32$
	ϕ	-58 ± 12
$f_0(1710)K^\pm$	c	0.24 ± 0.07
	ϕ	-22 ± 11
$\chi_{c0}K^\pm$	c	0.113 ± 0.017
	ϕ	45 ± 60
	δ	-12 ± 32
NR		
	b	-0.018 ± 0.023
a_{S0}	c	1.0 (fixed)
	ϕ	0 (fixed)
a_{S1}	c	1.00 ± 0.08
	ϕ	129 ± 6
a_{S2}	c	0.51 ± 0.08
	ϕ	-85 ± 8

TABLE X. Branching fractions (neglecting interference) for $B^+ \to K^0_S K^0_S K^+$. The $\mathcal{B}(B^+ \to RK^+)$ column gives the branching fractions to intermediate resonant states, corrected for secondary branching fractions obtained from Ref. [14]. Central values and uncertainties are for the global minimum only. See the text for discussion of the variations between the local minima.

Decay mode	$\mathcal{B}(B^+ \to K^0_S K^0_S K^+) \times FF_j(10^{-6})$	$\mathcal{B}(B^+ \to RK^+)(10^{-6})$
$f_0(980)K^+$	$14.7 \pm 2.8 \pm 1.8$	
$f_0(1500)K^+$	$0.42 \pm 0.22 \pm 0.58$	$20 \pm 10 \pm 27$
$f'_2(1525)K^+$	$0.61 \pm 0.21^{+0.12}_{-0.09}$	$2.8 \pm 0.9^{+0.5}_{-0.4}$
$f_0(1710)K^+$	$0.48^{+0.40}_{-0.24} \pm 0.11$	
$\chi_{c0}K^+$	$0.53 \pm 0.10 \pm 0.04$	$168 \pm 32 \pm 16$
NR (S wave)	$19.8 \pm 3.7 \pm 2.5$	

The CP-conserving isobar parameters for the global minimum solution are summarized in Table XI, and the branching fractions are given in Table XII. Table XIII shows the values of the CP-violating observables, with the central values taken from the global minimum, and the errors taken from likelihood scans. (Note that the second minimum is separated from the global minimum by $-2\Delta \ln\mathcal{L} = 3.9$, so the likelihood scan is not impacted by the local minima at the 1 standard deviation level.) In addition to $\beta_{\rm eff}$ and A_{CP}, we compute the quasi-two-body CP-violating parameter S, defined as

$$S_j \equiv -\frac{2\,\mathrm{Im}(e^{-2i\beta}\bar{a}_j a_j^*)}{|a_j|^2 + |\bar{a}_j|^2} = \frac{1 - b_j^2}{1 + b_j^2}\sin(2\beta_{\mathrm{eff},j}). \quad (47)$$

The fit fraction matrix for the best solution is given in the Appendix, and the correlation matrix of the isobar

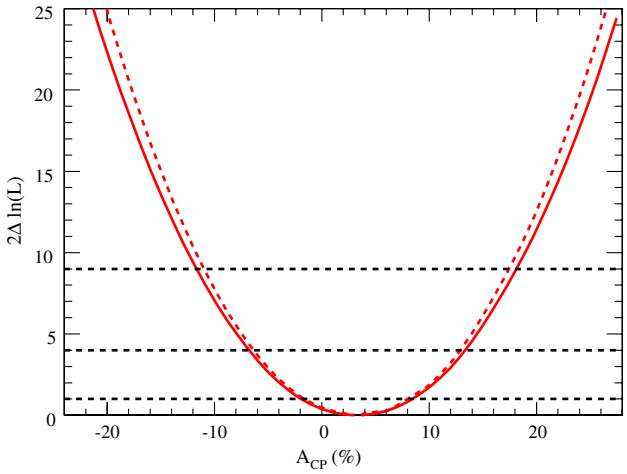

FIG. 14 (color online). Scan of $2\Delta\ln\mathcal{L}$, with (solid line) and without (dashed line) systematic uncertainties, as a function of A_{CP} in $B^+ \to K^0_S K^0_S K^+$.

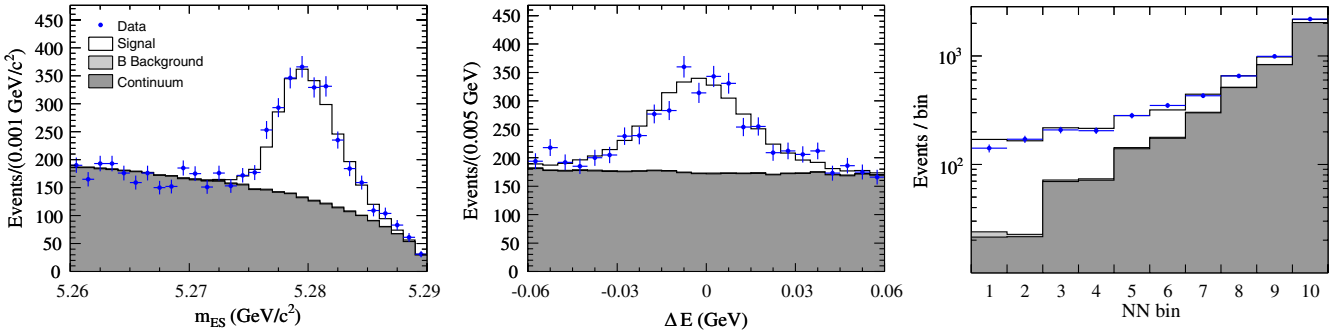

FIG. 15 (color online). Distributions of $m_{\rm ES}$ (left panel), ΔE (center panel), and NN output (right panel) for $B^0 \to K^+K^-K^0_S$, $K^0_S \to \pi^+\pi^-$. The NN output is shown in vertical log scale.

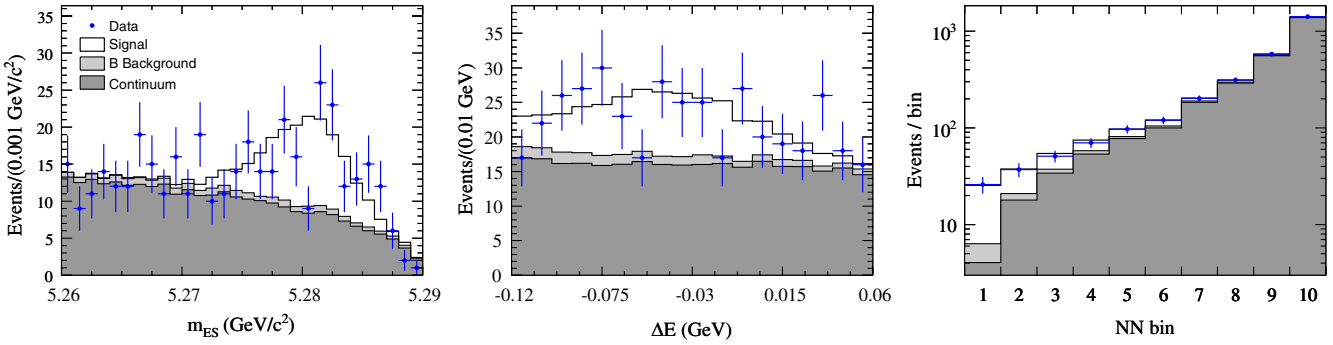

FIG. 16 (color online). Distributions of $m_{\rm ES}$ (left panel), ΔE (center panel), and NN output (right panel) for $B^0 \to K^+K^-K^0_S$, $K^0_S \to \pi^0\pi^0$. The signal in the $m_{\rm ES}$ and ΔE plots has been enhanced by requiring the NN output be 6 or less. The NN output is shown in vertical log scale.

parameters is given in Ref. [26]. The correlation matrix for the *CP*-violating observables is given in Table XIV.

The other minima all have consistent values for the $\phi(1020)$, $f'_2(1525)$, *P*-wave NR, and χ_{c0} fit fractions, but there are large variations in the fit fractions for the other states. Specifically, the fit fraction of the $f_0(980)$ varies between 19% and 41%, the fit fraction of the $f_0(1500)$ varies between 2% and 51%, the fit fraction of the $f_0(1710)$ varies between 2% and 27%, and the *S*-wave NR fit fraction varies between 34% and 120%. The signal yields for the different solutions, however, exhibit negligible variation. We calculate the inclusive branching fraction using only the yield in the $K^0_S \to \pi^+\pi^-$ channel. We find $\mathcal{B}(B^0 \to K^+K^-K^0) = (26.5 \pm 0.9 \pm 0.8) \times 10^{-6}$, or $\mathcal{B}(B^0 \to K^+K^-K^0) = (25.4 \pm 0.9 \pm 0.8) \times 10^{-6}$ if the χ_{c0} is excluded.

Likelihood scans for each of the $\beta_{\rm eff}$ and A_{CP} are shown in Figs. 19–21. $\beta_{\rm eff}$(other) is different from zero with 4.3σ significance. We can also distinguish between $\beta_{\rm eff}$ and the trigonometric reflection $90° - \beta_{\rm eff}$, due to the sensitivity of the DP analysis to interference between *S*-wave and *P*-wave amplitudes. We find that $\beta_{\rm eff}$(other) is favored over $90° - \beta_{\rm eff}$(other) with 4.8σ significance.

D. Interpretation

The value we measure for $A_{CP}(\phi K^+)$ is larger than the SM prediction, while $\beta_{\rm eff}(\phi K^0_S)$ is in excellent agreement with the SM. We can use the measured $A_{CP}(\phi K^+)$ and $\beta_{\rm eff}(\phi K^0_S)$ to put constraints on the amplitudes contributing to these decays. We assume isospin symmetry, so that the amplitudes for $B^+ \to \phi K^+$ and $B^0 \to \phi K^0_S$ are the same. We also assume that this amplitude, $\mathcal{A}$, can be written as the sum of two amplitudes, $\mathcal{A}_1$ and $\mathcal{A}_2$, where $\mathcal{A}_1$ is the dominant penguin amplitude. $\mathcal{A}_2$ is an arbitrary additional amplitude with a different weak phase, which could be a tree, *u* penguin, or new physics amplitude.

Then

$$\mathcal{A} = \mathcal{A}_1(1 + re^{i(\eta+\zeta)}), \quad \bar{\mathcal{A}} = \mathcal{A}_1(1 + re^{i(\eta-\zeta)}), \quad (48)$$

where r is the ratio $|\mathcal{A}_2/\mathcal{A}_1|$, and η and ζ are the relative strong and weak phases, respectively, between $\mathcal{A}_2$ and $\mathcal{A}_1$. The *CP* asymmetries in this case are

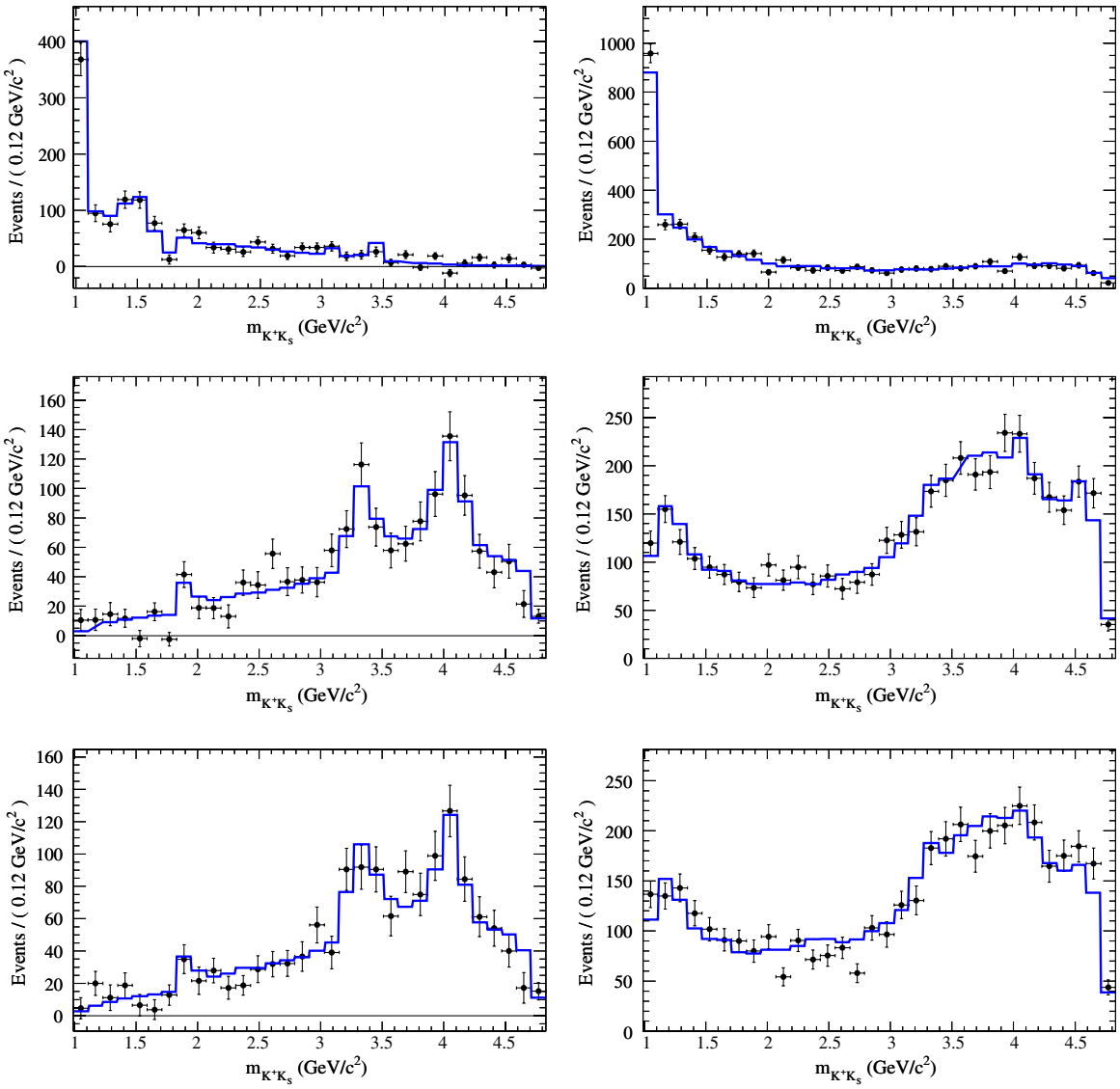

FIG. 17 (color online). Distributions of $m_{12} = m_{K^+K^-}$, $m_{23} = m_{K^-K^0_S}$, and $m_{13} = m_{K^+K^0_S}$, for signal-weighted (left column) and background-weighted (right column) $B^0 \to K^+K^-K^0_S$ candidates in data, $K^0_S \to \pi^+\pi^-$ only. The event weighting is performed using the ${}_s\mathcal{P}$lot method. The fit model (histograms) is shown superimposed over data (points). The two main peaks visible in the upper signal plot are due to the $\phi(1020)$ and $f_0(1500)/f_2'(1525)$. The leftmost peak in the middle and lower signal plots is due to D^-/D_s^- (background). The other hornlike peaks in those same plots are reflections from the $\phi(1020)$. The upper background plot has a $\phi(1020)$ peak (mainly due to continuum).

$$A_{CP}(\phi K^+) = \frac{2r\sin\zeta\sin\eta}{1 + 2r\cos\zeta\cos\eta + r^2} \tag{49}$$

and

$$\beta_{\rm eff}(\phi K^0_S) = \beta + \frac{1}{2}\arctan\left(\frac{2r\sin\zeta\cos\eta + r^2\sin(2\zeta)}{1 + 2r\cos\zeta\cos\eta + r^2\cos(2\zeta)}\right). \tag{50}$$

Note that $A_{CP}(\phi K^0_S) = A_{CP}(\phi K^+)$ under our assumptions. However, since the experimental precision on $A_{CP}(\phi K^0_S)$ is very poor compared to $A_{CP}(\phi K^+)$, we only include the more precise $A_{CP}(\phi K^+)$ measurement in our analysis. By combining the likelihood scans of $A_{CP}(\phi K^+)$ and $\beta_{\rm eff}(\phi K^0_S)$, we can put constraints on r, η, and ζ. Figure 22 shows the resulting constraints in the r-ζ, r-η, and η-ζ planes.

The nonzero value of $A_{CP}(\phi K^+)$ leads to $r = 0$ being disfavored by 2.8σ, with a value of approximately 0.1 favored for most values of ζ. There is little constraint on ζ and η, except that values of 0 or $\pm 180°$ are disfavored [because $A_{CP}(\phi K^+)$ is nonzero], and the first and third

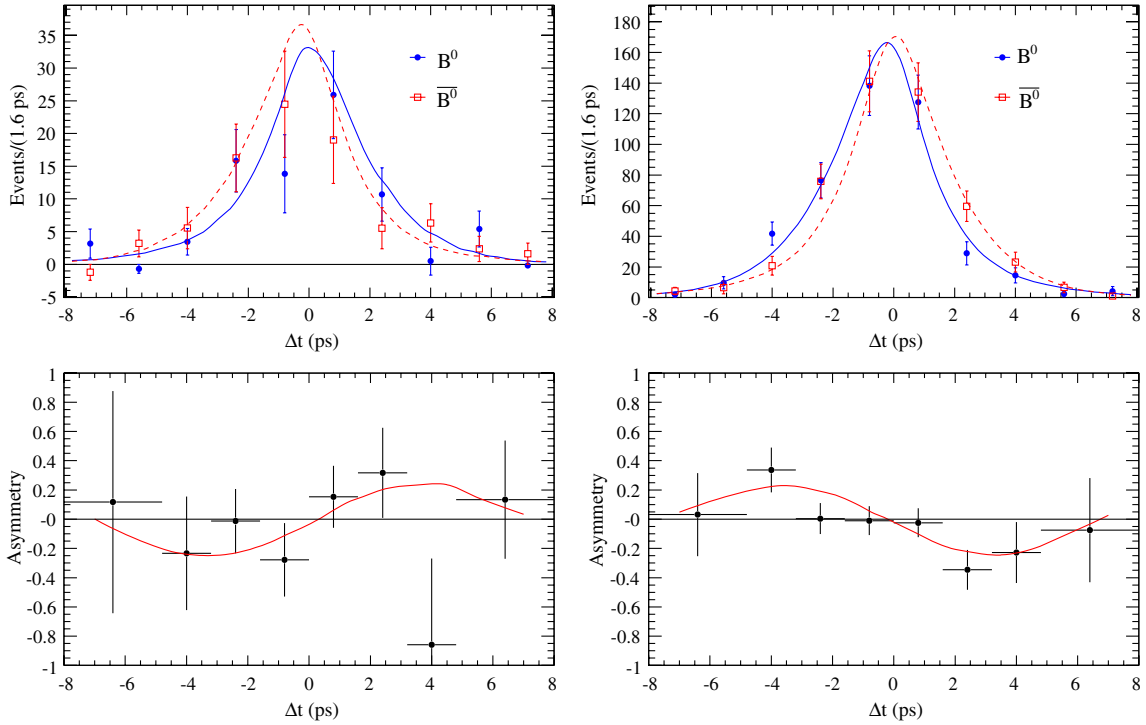

FIG. 18 (color online). Top: The Δt distributions for $B^0 \to K^+K^-K^0_S$ ($K^0_S \to \pi^+\pi^-$) signal events, in the $\phi(1020)$ region ($1.01 < m_{12} < 1.03$ GeV/c^2) (left panel) and $\phi(1020)$-excluded region (right panel). B^0 ($\bar{B}^0$) tagged events are shown as closed circles (open squares). The fit model for B^0 ($\bar{B}^0$) tagged events is shown by a solid (dashed) line. The data points are signal weighted using the ${}_s\mathcal{P}$lot method. Bottom: The asymmetry $(N_{B^0} - N_{\bar{B}^0})/(N_{B^0} + N_{\bar{B}^0})$ as a function of Δt, in the $\phi(1020)$ region (left panel) and $\phi(1020)$-excluded region (right panel). The points represent signal-weighted data, and the line is the fit model.

TABLE XI. *CP*-conserving isobar parameters [defined in Eq. (6)] for $B^0 \to K^+K^-K^0_S$, for the global minimum. The NR coefficients are defined in Eq. (28). Phases are given in degrees. Only statistical uncertainties are given.

Parameter		Value
$\phi(1020)K^0_S$	c	0.039 ± 0.005
	ϕ	20 ± 19
$f_0(980)K^0_S$	c	2.2 ± 0.5
	ϕ	40 ± 16
$f_0(1500)K^0_S$	c	0.22 ± 0.05
	ϕ	17 ± 16
$f'_2(1525)K^0_S$	c	$0.000\,80 \pm 0.000\,28$
	ϕ	53 ± 23
$f_0(1710)K^0_S$	c	0.72 ± 0.11
	ϕ	110 ± 11
$\chi_{c0}K^0_S$	c	0.144 ± 0.023
	ϕ	-17 ± 29
NR		
a_{S0}	c	1.0 (fixed)
	ϕ	0 (fixed)
a_{S1}	c	1.25 ± 0.25
	ϕ	-149 ± 9
a_{S2}	c	0.58 ± 0.22
	ϕ	56 ± 15
a_{P0}	c	1.22 ± 0.22
	ϕ	65 ± 13
a_{P1}	c	0.28 ± 0.18
	ϕ	-68 ± 28
a_{P2}	c	0.42 ± 0.16
	ϕ	-131 ± 25

TABLE XII. Branching fractions (neglecting interference) for $B^0 \to K^+K^-K^0_S$. The $\mathcal{B}(B^0 \to RK^0)$ column gives the branching fractions to intermediate resonant states, corrected for secondary branching fractions obtained from Ref. [14]. In addition to quoting the overall NR branching fraction, we quote the S-wave and P-wave NR branching fractions separately. Central values and uncertainties are for the global minimum only. See the text for discussion of the variations between the local minima.

Decay mode	$\mathcal{B}(B^0 \to K^+K^-K^0) \times FF_j$ (10^{-6})	$\mathcal{B}(B^0 \to RK^0)$ (10^{-6})
$\phi(1020)K^0$	$3.48 \pm 0.28^{+0.21}_{-0.14}$	$7.1 \pm 0.6^{+0.4}_{-0.3}$
$f_0(980)K^0$	$7.0^{+2.6}_{-1.8} \pm 2.4$	
$f_0(1500)K^0$	$0.57^{+0.25}_{-0.19} \pm 0.12$	$13.3^{+5.8}_{-4.4} \pm 3.2$
$f'_2(1525)K^0$	$0.13^{+0.12}_{-0.08} \pm 0.16$	$0.29^{+0.27}_{-0.18} \pm 0.36$
$f_0(1710)K^0$	$4.4 \pm 0.7 \pm 0.5$	
$\chi_{c0}K^0$	$0.90 \pm 0.18 \pm 0.06$	$148 \pm 30 \pm 13$
NR	$33 \pm 5 \pm 9$	
NR (S wave)	$30 \pm 5 \pm 8$	
NR (P wave)	$3.1 \pm 0.7 \pm 0.4$	

TABLE XIII. CP-violating parameters $\beta_{\rm eff}$, A_{CP}, and S for $B^0 \to K^+K^-K^0_S$. Central values correspond to the global minimum. Statistical uncertainties for $\beta_{\rm eff}$ and A_{CP} are determined from likelihood scans.

Component	$\beta_{\rm eff}$ (deg)	$A_{CP}(=-C)$ (%)	S
$\phi(1020)K^0_S$	$21 \pm 6 \pm 2$	$-5 \pm 18 \pm 5$	$0.66 \pm 0.17 \pm 0.07$
$f_0(980)K^0_S$	$18 \pm 6 \pm 4$	$-28 \pm 24 \pm 9$	$0.55 \pm 0.18 \pm 0.12$
Other	$20.3 \pm 4.3 \pm 1.2$	$-2 \pm 9 \pm 3$	$0.65 \pm 0.12 \pm 0.03$

TABLE XIV. Statistical correlation matrix for the CP-violating parameters $\beta_{\rm eff}$ and A_{CP} for $B^0 \to K^+K^-K^0_S$. The matrix corresponds to the global minimum solution.

	$\beta_{\rm eff}(\phi(1020))$	$\beta_{\rm eff}(f_0(980))$	$\beta_{\rm eff}$ (other)	$A_{CP}(\phi(1020))$	$A_{CP}(f_0(980))$	A_{CP} (other)
$\beta_{\rm eff}(\phi(1020))$	1.00	0.38	0.15	0.21	−0.44	−0.32
$\beta_{\rm eff}(f_0(980))$		1.00	0.63	−0.10	0.05	−0.33
$\beta_{\rm eff}$ (other)			1.00	−0.13	0.47	0.14
$A_{CP}(\phi(1020))$				1.00	−0.25	−0.14
$A_{CP}(f_0(980))$					1.00	0.60
A_{CP} (other)						1.00

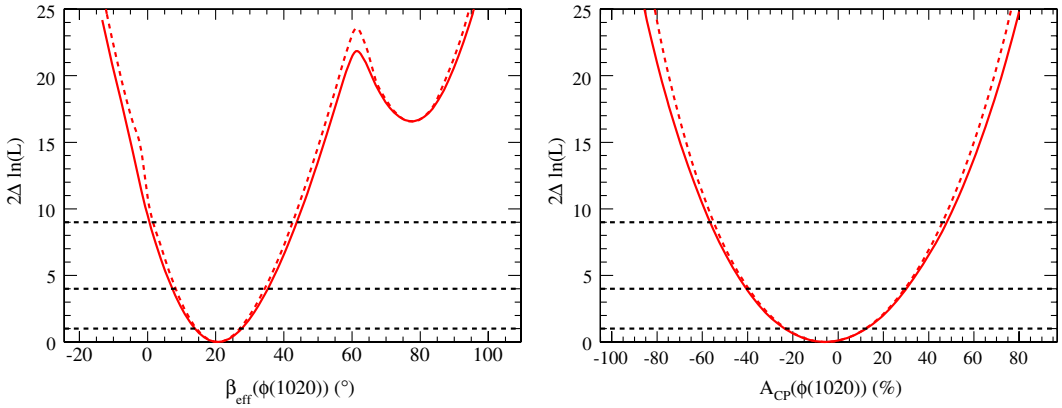

FIG. 19 (color online). Scan of $2\Delta \ln \mathcal{L}$, with (solid line) and without (dashed line) systematic uncertainties, as a function of $\beta_{\rm eff}$ (left panel) and A_{CP} (right panel) for $B^0 \to \phi(1020)K^0_S$.

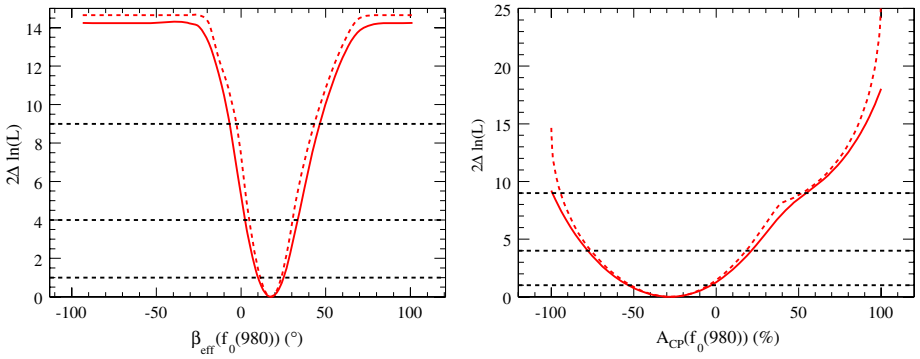

FIG. 20 (color online). Scan of $2\Delta \ln\mathcal{L}$, with (solid line) and without (dashed line) systematic uncertainties, as a function of $\beta_{\rm eff}$ (left panel) and A_{CP} (right panel) for $B^0 \to f_0(980)K^0_S$. The flat region of the $\beta_{\rm eff}$ scan is caused by the $A_{CP}(f_0(980))$ going to -100% in this region, in which case $\beta_{\rm eff}$ becomes an irrelevant parameter.

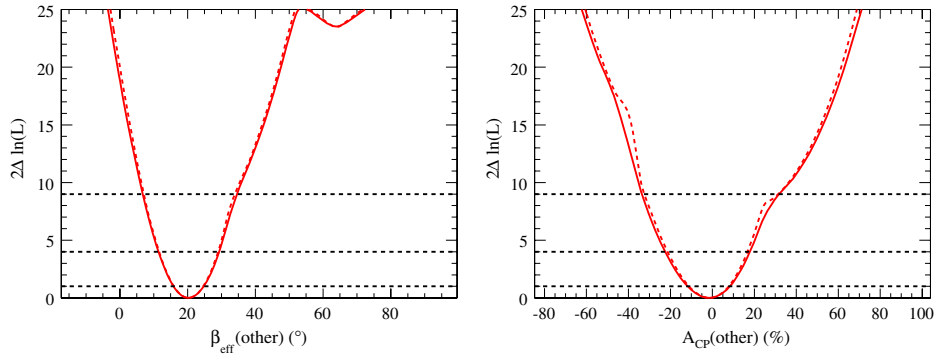

FIG. 21 (color online). Scan of $2\Delta \ln\mathcal{L}$, with (solid line) and without (dashed line) systematic uncertainties, as a function of $\beta_{\rm eff}$ (left panel) and A_{CP} (right panel) for $B^0 \to K^+K^-K^0_S$, excluding the $\phi(1020)$, $f_0(980)$, and χ_{c0}.

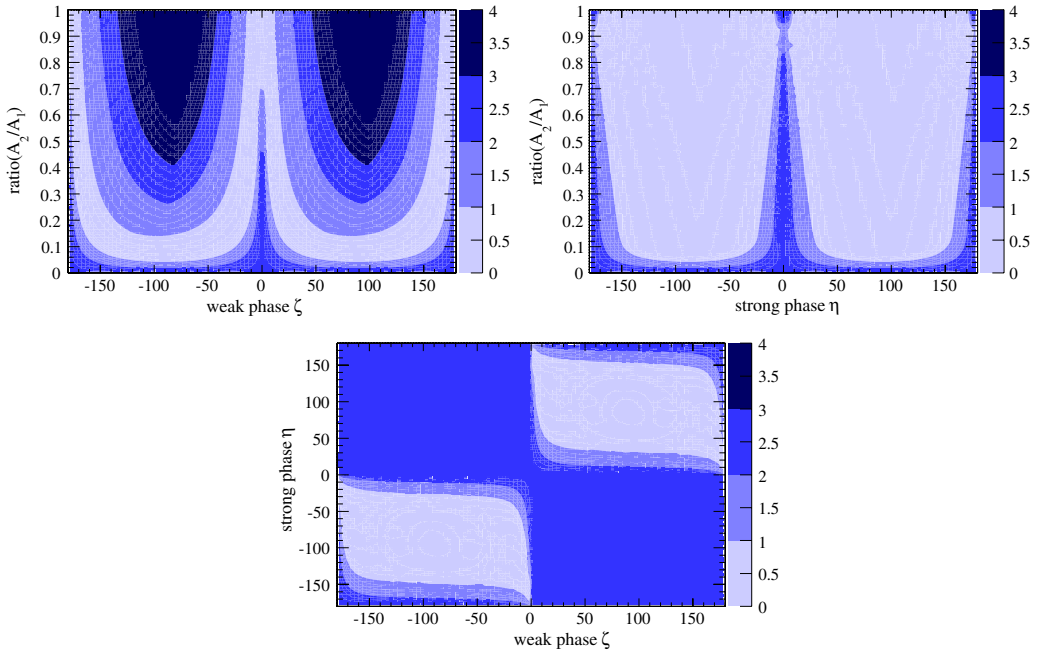

FIG. 22 (color online). Constraints on the amplitude ratio $|\mathcal{A}_2/\mathcal{A}_1|$ and the relative strong and weak phases, η and ζ, between $\mathcal{A}_1$ and $\mathcal{A}_2$, for $B^+ \to \phi K^+$ and $B^0 \to \phi K^0_S$ decays. The shaded areas, from light to dark, show the 1σ, 2σ, 3σ, and 4σ allowed regions.

quadrants of the η-ζ plane are favored [because $A_{CP}(\phi K^+)$ is positive].

VIII. SYSTEMATIC UNCERTAINTIES

The systematic uncertainties for $B^+ \to K^+K^-K^+$, $B^+ \to K^0_S K^0_S K^+$, and $B^0 \to K^+K^-K^0_S$ parameters are summarized in Tables XV, XVI, and XVII, respectively. For each decay mode, the systematic uncertainties are assessed only for the best solution.

We vary the masses and widths of the resonances in the signal model by their errors as given in Table I. In addition, we vary the Blatt-Weisskopf radii of any nonscalar resonances, and change the Blatt-Weisskopf radius of the B meson from 0 to 1.5 $(\mathrm{GeV}/c)^{-1}$. We take the observed differences in any fit parameters as systematic uncertainties (listed in the "Line shape" column in Tables XV, XVI, and XVII).

We vary any $B\bar{B}$ background yields that are fixed in the nominal fit. If the $B\bar{B}$ class contains only a single decay mode, the yield is varied according to the uncertainty on the world average of its branching fraction. If the $B\bar{B}$ class contains multiple decay modes, then we vary its yield by 50%. The CP asymmetries of the $B\bar{B}$ background classes are also varied, either by the uncertainty on the world average or by a conservative estimate. Systematic uncertainties are also assigned due to the limited sizes of the $B\bar{B}$ MC samples, which affects the $B\bar{B}$ PDF shapes. We also vary signal and continuum background PDF parameters that are fixed in the nominal fits. This includes the

TABLE XV. Summary of systematic uncertainties for $B^+ \to K^+K^-K^+$ parameters. Errors on phases, A_{CP}'s, and branching fractions are given in degrees, percent, and units of 10^{-6}, respectively.

Parameter	Line shape	Fixed PDF params	Other	Add resonances	Fit bias	Total
$\Delta\phi(\phi(1020))$	3	1	0	2	2	4
$\Delta\phi(f_0(980))$	2	1	0	6	1	6
$\Delta\phi(f'_2(1525))$	1	0	0	3	1	3
$\Delta\phi(\chi_{c0})$	1	1	0	1	1	2
$A_{CP}(\phi(1020))$	0.2	0.2	1.0	0.3	0.7	1.3
$A_{CP}(f_0(980))$	3	1	1	2	1	4
$A_{CP}(f'_2(1525))$	1	1	1	3	1	4
A_{CP} (NR)	1.1	0.4	1.0	0.8	0.7	1.9
$\mathcal{B}(\phi(1020))$	0.20	0.04	0.11	0.14	0.08	0.29
$\mathcal{B}(f_0(980))$	1.2	0.1	0.3	2.5	0.4	2.8
$\mathcal{B}(f_0(1500))$	0.06	0.02	0.02	0.52	0.02	0.52
$\mathcal{B}(f'_2(1525))$	0.05	0.01	0.02	0.07	0.10	0.13
$\mathcal{B}(f_0(1710))$	0.08	0.04	0.03	0.49	0.05	0.50
$\mathcal{B}(\chi_{c0})$	0.01	0.01	0.03	0.02	0.04	0.06
$\mathcal{B}$ (NR)	1.0	0.2	0.5	7.4	0.3	7.6
$\mathcal{B}$ (NR (S wave))	13	2	1	23	2	27
$\mathcal{B}$ (NR (P wave))	10	2	1	25	3	27
$\mathcal{B}$ (total)	0.0	0.2	0.8	0.1	0.4	0.9
$\mathcal{B}$ (charmless)	0.0	0.2	0.8	0.1	0.3	0.9

TABLE XVI. Summary of systematic uncertainties for $B^+ \to K^0_S K^0_S K^+$ parameters. Errors on A_{CP} and branching fractions are given in percent and units of 10^{-6}, respectively.

Parameter	Line shape	Fixed PDF params	Other	Add resonances	Fit bias	Total
A_{CP}	0	0	1	0	1	2
$\mathcal{B}(f_0(980))$	1.4	0.3	0.3	1.0	0.4	1.8
$\mathcal{B}(f_0(1500))$	0.05	0.03	0.01	0.57	0.04	0.58
$\mathcal{B}(f'_2(1525))$	0.06	0.02	0.02	0.07	0.03	0.10
$\mathcal{B}(f_0(1710))$	0.06	0.04	0.01	0.02	0.08	0.11
$\mathcal{B}(\chi_{c0})$	0.01	0.01	0.01	0.00	0.03	0.04
$\mathcal{B}$ (NR (S wave))	1.3	0.6	0.4	2.0	0.2	2.5
$\mathcal{B}$ (total)	0.0	0.2	0.2	0.0	0.0	0.3
$\mathcal{B}$ (charmless)	0.0	0.2	0.2	0.0	0.0	0.3

TABLE XVII. Summary of systematic uncertainties for $B^0 \to K^+K^-K^0_S$ parameters. Errors on angles, A_{CP}'s, and branching fractions are given in degrees, percent, and units of 10^{-6}, respectively.

Parameter	Line shape	Fixed PDF params	Other	Add resonances	Fit bias	Total
$\beta_{\rm eff}(\phi(1020))$	2	1	0	2	0	2
$\beta_{\rm eff}(f_0(980))$	1	1	0	4	0	4
$\beta_{\rm eff}$ (other)	0.7	0.4	0.2	0.8	0.4	1.2
$A_{CP}(\phi(1020))$	2	2	2	2	3	5
$A_{CP}(f_0(980))$	6	3	2	5	2	9
A_{CP} (other)	1	1	1	2	1	3
$\mathcal{B}(\phi(1020))$	0.13	0.05	0.08	0.05	0.03	0.18
$\mathcal{B}(f_0(980))$	1.3	0.3	0.1	2.0	0.1	2.4
$\mathcal{B}(f_0(1500))$	0.04	0.02	0.02	0.10	0.03	0.12
$\mathcal{B}(f'_2(1525))$	0.02	0.01	0.00	0.15	0.02	0.16
$\mathcal{B}(f_0(1710))$	0.3	0.1	0.1	0.4	0.1	0.5
$\mathcal{B}(\chi_{c0})$	0.02	0.02	0.02	0.01	0.04	0.06
$\mathcal{B}$ (NR(total))	2	1	1	8	1	9
$\mathcal{B}$ (NR (S wave))	2	1	1	8	1	8
$\mathcal{B}$ (NR (P wave))	0.1	0.2	0.1	0.3	0.1	0.4
$\mathcal{B}$ (total)	0.0	0.4	0.7	0.0	0.1	0.8
$\mathcal{B}$ (charmless)	0.1	0.4	0.6	0.0	0.2	0.8

parameters of the Δt resolution function and the mistag rate. An additional systematic uncertainty is contributed by the limited size of the data sideband sample used to create the continuum DP PDFs. These systematic uncertainties are listed under "Fixed PDF params" in Tables XV, XVI, and XVII.

Biases in the fit procedure are studied by performing hundreds of pseudoexperiments using MC events passed through a GEANT4-based detector simulation. We do not correct for any observed biases, but instead assign systematic uncertainties, listed under "Fit bias" in Tables XV, XVI, and XVII.

We also study the effect of additional resonances that are not included in our nominal isobar models (see Sec. VI). We test for the $f_0(1370)$, $a^0_0(1450)$, $f_2(1270)$, $f_2(2010)$, and $f_2(2300)$ in each mode. We also test for the $\phi(1680)$ in $B^+ \to K^+K^-K^+$ and $B^0 \to K^+K^-K^0_S$, and the $a^\pm_0(980)$ and $a^\pm_0(1450)$ in $B^+ \to K^0_SK^0_SK^+$ and $B^0 \to K^+K^-K^0_S$. These resonances are modeled by RBW line shapes, except for the $a^\pm_0(980)$, which is modeled by a Flatté line shape. We first fit to data including these additional resonances in the model. Then, using this fit result, we generate a large number of data-sized simulated data sets. We then fit to these simulated data sets with and without the additional resonances in the signal model, and take the observed differences as a systematic uncertainty. This is listed as "Add resonances" in Tables XV, XVI, and XVII. In $B^+ \to K^+K^-K^+$, the addition of the $f_0(1370)$ causes solution II to be the global mininum rather than solution I, so we do not assign a systematic uncertainty for it.

Additional systematic uncertainties are listed as "Other" in Tables XV, XVI, and XVII. Systematic uncertainties are assessed for tracking efficiency, K^0_S reconstruction, and $K^\pm$ PID. We also compute a systematic uncertainty due to the limited sizes of the MC samples used to calculate the signal efficiency as a function of DP position. We assign a 1% systematic uncertainty due to possible detector charge asymmetries not properly modeled in the detector simulation. For the *CP*-violating parameters in $B^0 \to K^+K^-K^0_S$, we assign a systematic uncertainty due to the interference between CKM-favored and CKM-suppressed tag-side B decays [27].

IX. SUMMARY

We have performed amplitude analyses of the decays $B^+ \to K^+K^-K^+$ and $B^+ \to K^0_SK^0_SK^+$, and a time-dependent amplitude analysis of $B^0 \to K^+K^-K^0_S$, using a data sample of approximately 470×10^6 $B\bar{B}$ decays.

For $B^+ \to K^+K^-K^+$, we find two solutions separated by 5.6 units of $-2\ln\mathcal{L}$. The favored solution has a direct *CP* asymmetry in $B^+ \to \phi(1020)K^+$ of $A_{CP} = (12.8 \pm 4.4 \pm 1.3)\%$. A likelihood scan shows that A_{CP} differs from 0 by 2.8σ, including systematic uncertainties. This can be compared with the SM expectation of $A_{CP} = (0.0\text{–}4.7)\%$. For $B^0 \to K^+K^-K^0_S$, we find five solutions, and determine $\beta_{\rm eff}(\phi K^0_S) = (21 \pm 6 \pm 2)^\circ$ from a likelihood scan. Excluding the $\phi(1020)K^0_S$ and $f_0(980)K^0_S$ contributions, we measure $\beta_{\rm eff} = (20.3 \pm 4.3 \pm 1.2)^\circ$ for the remaining $B^0 \to K^+K^-K^0_S$ decays, and exclude the trigonometric reflection $90^\circ - \beta_{\rm eff}$ at 4.8σ, including systematic uncertainties. For $B^+ \to K^0_SK^0_SK^+$, there is insufficient data to fully constrain the many complex amplitudes in the DP model. However, from a likelihood scan we measure an

overall direct CP asymmetry of $A_{CP} = (4^{+4}_{-5} \pm 2)\%$. By combining the $A_{CP}(\phi K^{\pm})$ and $\beta_{\rm eff}(\phi K^0_S)$ results and assuming isospin symmetry, we place constraints on the possible SM and NP amplitudes contributing to these decays.

We also study the DP structure of the three $B \to KKK$ modes, by means of an angular-moment analysis. This includes the first ever DP analysis of $B^+ \to K^0_S K^0_S K^+$. To describe the large nonresonant contributions seen in the three $B^+ \to K^+K^-K^+$ modes, we introduce a polynomial model that includes explicit S-wave and P-wave terms and allows for phase motion. We conclude that the hypothetical particle dubbed the $f_X(1500)$ is not a single scalar resonance, but instead can be described by the sum of the well-established resonances $f_0(1500)$, $f'_2(1525)$, and $f_0(1710)$.

ACKNOWLEDGMENTS

We are grateful for the extraordinary contributions of our PEP-II colleagues in achieving the excellent luminosity and machine conditions that have made this work possible. The success of this project also relies critically on the expertise and dedication of the computing organizations that support *BABAR*. The collaborating institutions wish to thank SLAC for its support and the kind hospitality extended to them. This work is supported by the U.S. Department of Energy and the National Science Foundation, the Natural Sciences and Engineering Research Council (Canada), the Commissariat à l'Energie Atomique and Institut National de Physique Nucléaire et de Physique des Particules (France), the Bundesministerium für Bildung und Forschung and Deutsche Forschungsgemeinschaft (Germany), the Istituto Nazionale di Fisica Nucleare (Italy), the Foundation for Fundamental Research on Matter (The Netherlands), the Research Council of Norway, the Ministry of Education and Science of the Russian Federation, the Ministerio de Ciencia e Innovación (Spain), and the Science and Technology Facilities Council (United Kingdom). Individuals have received support from the Marie-Curie IEF program (European Union) and the A. P. Sloan Foundation (USA).

APPENDIX

We give Tables XVIII, XIX, XX, and XXI of the interference fit fractions FF_{jk}, defined in Eq. (8).

TABLE XVIII. Values of the interference fit fractions FF_{jk} for $B^+ \to K^+K^-K^+$, solution I. The diagonal terms FF_{jj} are the ordinary fit fractions FF_j, which sum to 272%. The NR component is split into S-wave and P-wave parts for these calculations. Values are given in percent.

	$\phi(1020)$	$f_0(980)$	$f_0(1500)$	$f'_2(1525)$	$f_0(1710)$	χ_{c0}	NR (S wave)	NR (P wave)
$\phi(1020)$	12.9	−0.1	0.0	0.0	0.1	−0.0	−7.4	8.2
$f_0(980)$		27.2	−4.7	−0.0	−5.4	−1.0	−0.8	−3.7
$f_0(1500)$			2.1	0.0	2.3	0.1	3.1	−0.8
$f'_2(1525)$				2.0	0.1	−0.0	−0.0	0.7
$f_0(1710)$					3.2	−0.1	−13.5	4.9
χ_{c0}						3.2	3.3	−1.8
NR (S wave)							151.4	−155.0
NR (P wave)								69.4

TABLE XIX. Values of the interference fit fractions FF_{jk} for $B^+ \to K^+K^-K^+$, solution II. The diagonal terms FF_{jj} are the ordinary fit fractions FF_j, which sum to 174%. The NR component is split into S-wave and P-wave parts for these calculations. Values are given in percent.

	$\phi(1020)$	$f_0(980)$	$f_0(1500)$	$f'_2(1525)$	$f_0(1710)$	χ_{c0}	NR (S wave)	NR (P wave)
$\phi(1020)$	12.3	−0.3	−0.1	−0.0	−0.1	−0.1	−1.5	5.1
$f_0(980)$		12.5	1.5	0.1	3.9	0.6	−40.6	−10.2
$f_0(1500)$			2.6	−0.0	2.3	0.1	−3.5	−0.0
$f'_2(1525)$				1.5	0.0	−0.0	−0.3	0.7
$f_0(1710)$					2.5	−0.0	−11.6	−2.4
χ_{c0}						3.6	−1.5	0.5
NR (S wave)							91.1	−17.2
NR (P wave)								48.2

TABLE XX. Values of the interference fit fractions FF_{jk} for $B^+ \to K^0_S K^0_S K^+$, for the global minimum. The diagonal terms FF_{jj} are the ordinary fit fractions FF_j, which sum to 345%. Values are given in percent.

	$f_0(980)$	$f_0(1500)$	$f'_2(1525)$	$f_0(1710)$	χ_{c0}	NR (S wave)
$f_0(980)$	139.0	−19.2	0.0	−12.4	−1.0	−217.0
$f_0(1500)$		4.0	−0.0	4.1	0.2	9.5
$f'_2(1525)$			5.7	−0.0	−0.0	−0.0
$f_0(1710)$				4.5	0.1	−9.2
χ_{c0}					5.0	−0.0
NR (S wave)						186.5

TABLE XXI. Values of the interference fit fractions FF_{jk} for $B^0 \to K^+ K^- K^0_S$, for the global minimum. The diagonal terms FF_{jj} are the ordinary fit fractions FF_j, which sum to 188%. The NR component is split into S-wave and P-wave parts for these calculations. Values are given in percent.

	$\phi(1020)$	$f_0(980)$	$f_0(1500)$	$f'_2(1525)$	$f_0(1710)$	χ_{c0}	NR (S wave)	NR (P wave)
$\phi(1020)$	13.1	0.0	0.0	0.0	0.0	0.0	0.0	0.2
$f_0(980)$		26.3	0.1	−0.0	14.4	−0.7	−81.2	0.0
$f_0(1500)$			2.1	−0.0	5.3	−0.1	−0.7	0.0
$f'_2(1525)$				0.5	−0.0	0.0	0.0	0.0
$f_0(1710)$					16.7	−0.2	−27.0	0.0
χ_{c0}						3.4	1.6	0.0
NR (S wave)							114.5	0.0
NR (P wave)								11.7

[1] B. Aubert *et al.* (*BABAR* Collaboration), Phys. Rev. D **79**, 072009 (2009).
[2] K.-F. Chen *et al.* (Belle Collaboration), Phys. Rev. Lett. **98**, 031802 (2007).
[3] M. Beneke, Phys. Lett. B **620**, 143 (2005).
[4] H.-Y. Cheng, C.-K. Chua, and A. Soni, Phys. Rev. D **72**, 014006 (2005).
[5] H.-n. Li and S. Mishima, Phys. Rev. D **74**, 094020 (2006).
[6] M. Beneke and M. Neubert, Nucl. Phys. **B675**, 333 (2003).
[7] B. Aubert *et al.* (*BABAR* Collaboration), Phys. Rev. D **74**, 032003 (2006).
[8] A. Garmash *et al.* (Belle Collaboration), Phys. Rev. D **71**, 092003 (2005).
[9] Y. Nakahama *et al.* (Belle Collaboration), Phys. Rev. D **82**, 073011 (2010).
[10] B. Aubert *et al.* (*BABAR* Collaboration), Phys. Rev. Lett. **99**, 161802 (2007).
[11] J. P. Lees *et al.* (*BABAR* Collaboration), Phys. Rev. D **85**, 054023 (2012).
[12] J. Blatt and V. E. Weisskopf, *Theoretical Nuclear Physics* (Wiley, New York, 1952).
[13] C. Zemach, Phys. Rev. **133**, B1201 (1964).
[14] K. Nakamura *et al.* (Particle Data Group), J. Phys. G **37**, 075021 (2010).
[15] M. Ablikim *et al.* (BES Collaboration), Phys. Lett. B **607**, 243 (2005).
[16] S. M. Flatté, Phys. Lett. **63B**, 224 (1976).
[17] B. Aubert *et al.* (*BABAR* Collaboration), Nucl. Instrum. Methods Phys. Res., Sect. A **479**, 1 (2002).
[18] S. Agostinelli *et al.* (GEANT4 Collaboration), Nucl. Instrum. Methods Phys. Res., Sect. A **506**, 250 (2003).
[19] R. J. Barlow, Nucl. Instrum. Methods Phys. Res., Sect. A **297**, 496 (1990).
[20] H. Albrecht *et al.* (ARGUS Collaboration), Z. Phys. C **48**, 543 (1990).
[21] F. James and M. Roos, Comput. Phys. Commun. **10**, 343 (1975).
[22] A. Genz and A. Malik, J. Comput. Appl. Math. **6**, 295 (1980).
[23] B. Aubert *et al.* (*BABAR* Collaboration), Phys. Rev. Lett. **99**, 221801 (2007).
[24] B. Aubert *et al.* (*BABAR* Collaboration), Phys. Rev. D **79**, 051101 (2009).
[25] M. Pivk and F. R. Le Diberder, Nucl. Instrum. Methods Phys. Res., Sect. A **555**, 356 (2005).
[26] See Supplemental Material at http://link.aps.org/supplemental/10.1103/PhysRevD.85.112010 for the correlation matrices of the isobar parameters.
[27] O. Long, M. Baak, R. N. Cahn, and D. P. Kirkby, Phys. Rev. D **68**, 034010 (2003).